Title: REM sleep prefrontal ripple chains mediate distinct cortical-hippocampal reactivation patterns compared to NREM ripples

Authors: Justin D. Shin[1], Michael Satchell[1], Paul Miller[1], Shantanu P. Jadhav[1]*

5 **Affiliations:** [1]Neuroscience Program, Department of Psychology, and Volen National Center for Complex Systems, Brandeis University; Waltham, MA 02453, USA

*Corresponding author; Email: shantanu@brandeis.edu

SUMMARY

REM (rapid eye movement) and non-REM (NREM) sleep stages are both critical for systems memory consolidation in hippocampal-cortical circuits. However, the physiological mechanisms underlying REM memory processes remain relatively unclear compared to NREM memory reactivation. Here we report, in rodents, the existence of prefrontal cortical (PFC) high-frequency ripple chains in REM sleep during consolidation of recently acquired spatial memory. High-density tetrode recordings in hippocampal area CA1 and PFC reveal that, in contrast to NREM cortical ripples, REM cortical ripples occur in characteristic chains that are phase modulated by theta oscillations in phasic REM sleep, corresponding to increased CA1-PFC theta coherence and delineating periods of enhanced hippocampal-cortical communication. REM ripple chains sequentially organize sparse PFC ensemble reactivation of behavioral activity during periods of local suppression, distinct from widespread reactivation bursts during NREM ripples. REM ripple chains also selectively engage CA1 neuronal populations that shift preferred theta-phase from behavior to REM sleep. Co-reactivation of PFC and CA1 neurons during REM ripple chains was linked to CA1 activity suppression during NREM PFC ripples, and to differential changes in CA1 neuronal firing rates in sleep, suggesting REM-driven regulation of hippocampal excitability. A cortical network model incorporating the effects of acetylcholine can reproduce the distinct REM and NREM activity patterns, providing a mechanistic basis for widespread coactivity during NREM cortical ripples, compared to sparse, temporally extended reactivation on a background of local suppression during REM ripple chains. Overall, these findings establish a role for PFC ripples in regulating distinct dual sleep stage cortical-hippocampal reactivation patterns.

KEYWORDS

Hippocampus, Prefrontal Cortex, REM sleep, NREM, Reactivation, Excitability, Ripples, Consolidation

INTRODUCTION

Rapid eye movement (REM) sleep, often referred to as paradoxical sleep due to its electrophysiological similarities to wakefulness, is a relatively transient stage of sleep that occurs after NREM sleep stages in cycles, and plays a crucial role in a wide range of brain functions.[1,2] Although largely appreciated for its role in emotional processing, recent evidence has highlighted its role in the consolidation of spatial, declarative, and procedural memory, indicating a broader function of REM sleep in mnemonic processing.[3,4] Importantly, REM dysregulation is associated with memory deficits and is thought to contribute to the progression of neuropsychiatric disorders and neurodegenerative diseases such as depression and dementia, highlighting the critical need for a deeper understanding of this sleep state to benefit human health.[5]

Primary models of systems memory consolidation, including the standard two-stage theory of consolidation or multiple trace theory,[6-8] rest under the assumption of cooperative hippocampal-cortical reactivation during sleep to transform initially encoded episodic hippocampal representations into broadly distributed hippocampal-cortical representations for long-term storage and semantic memory formation. In support of this view, several rodent and human studies have confirmed that, in non-rapid eye movement (NREM) sleep, coordination of hippocampal sharp-wave ripples (SWRs) with cortical slow oscillations (1-4 Hz), spindles (12-16 Hz), and ripples (150-250 Hz) underlies the neurophysiological mechanism supporting consolidation.[9-12] While the role of offline memory reactivation in the hippocampus and prefrontal cortex (PFC) during NREM sleep has been extensively studied in relation to memory function, the precise mechanisms through which REM sleep contributes to these processes, particularly in the context of hippocampal-cortical interactions, is still unclear. REM sleep is characterized by high theta-delta ratio,[13,14] and hippocampal SWRs are primarily reported in NREM states with relatively low theta power. Hippocampal theta rhythms during REM sleep have been shown to be important for memory consolidation,[15] and corresponding phasic theta activity bursts during REM are often coupled with elevated gamma and cortical high-frequency oscillation (ripple) power, potentially organizing neural activity in distributed circuits for mnemonic processing.[16-20] Furthermore, REM sleep is associated with a unique neuromodulatory landscape that is conducive for the induction of plasticity within and across circuits.[21] However, the role of REM sleep cortical oscillations, whether they are coordinated with hippocampal activity patterns or with cortical-hippocampal reactivation, and the relationship between REM and NREM activity for dual sleep state regulation of reactivation and excitability are all open questions.

Cortical ripples (high-frequency or fast oscillations, ~150-250 Hz) have been reported in NREM sleep,[22-24] and our recent study showed that independent PFC ripples that are dissociated from hippocampal SWRs are prevalent in NREM sleep and mediate suppression of hippocampal activity and reactivation, potentially facilitating the selection and consolidation of specific hippocampal memory ensembles, while facilitating local cortical reactivation.[23] These ripples likely reflect intracortical processing that occurs independently of hippocampal input, allowing for interference-free consolidation of memory representations within cortical circuits.[25] Previous studies have also established these high-frequency cortical oscillations (termed HFOs) along with gamma oscillations in REM sleep,[17,19,20,26] but an explicit examination of these events, and how they impact cortical and hippocampal reactivation is not known. Furthermore, how NREM and REM

sleep activity patterns may together complementarily shape the development and refinement of cortical-hippocampal ensembles to support learning is unclear. Therefore, we used high-density electrophysiological recordings in PFC and CA1 during learning and subsequent sleep to investigate whether and how coordinated activity during REM sleep may drive circuit changes underlying systems memory consolidation, and whether prefrontal and hippocampal dynamics differ during cortical ripple activity patterns in NREM and REM sleep.

RESULTS

High-frequency events in PFC during REM sleep

We simultaneously recorded local field potential (LFP) and neuronal populations in CA1 (n = 1,468) and PFC (n = 1,151) from animals (n = 10 rats) during REM sleep (**Figure S1A, Table S1**, REM duration = 164.6 ± 10.8 s/epoch for epochs included in analysis) throughout the course of learning a spatial memory task that requires hippocampal-prefrontal interactions[27,28] (**Figures S1A,B**). Activity was continuously acquired across multiple run (8 epochs) and sleep (9 epochs) sessions during learning.[28] We separated NREM and REM sleep based on theta-to-delta (TD) ratio,[13,14] and find coherent shifts in TD ratio across CA1 and PFC at the onset and offset of REM sleep (**Figures 1A** and **S1B,C**), as well as higher movement and intracranial EMG during wake as compared to REM sleep, validating the behavioral state designations (**Figures S1C-F**). To investigate the high-frequency component of phasic burst activity in PFC, cortical ripples during NREM and REM sleep were detected as transient events in the 150-250 Hz range, as previously described[23] (**Figures 1B,C** and **S1G,H**), with similar criteria used to detect cortical ripple events in NREM and REM states. Cortical ripple rates during REM were higher than NREM (**Figure 1E**), and REM ripples were associated with elevated theta and gamma power,[19,26] in contrast to spindle- and slow oscillation-coupled ripple events in NREM[23,29] (**Figure 1D**). Interestingly, examining the difference in autocorrelation peaks and inter-event-intervals (IEI), we find that REM ripples often recur at intervals of ~130 ms (**Figures 1F**,**G**) as ripple "chains", which is consistent with theta frequency modulation and elevated theta power during these events (**Figure 1D**). REM ripples are associated with fast, theta timescale fluctuations in PFC population activity during periods of locally reduced activity, as evidenced by the overall decrease in population activity during these events (**Figure 1H**). This phenomenon was also present when using different parameters for ripple detection or REM sleep designation (**Figures S1J-L**). Conversely, NREM cortical ripples were associated with a singular burst of activity spanning several hundred milliseconds[23] (**Figures 1I** and **S1I**). Thus, these findings establish distinct ripple-associated activity profiles in PFC that may underlie differential processing of memory related information during NREM and REM sleep.

Coupling of theta, gamma, and prefrontal ripple oscillations in REM sleep

Theta-gamma phase-amplitude coupling (PAC) is one of the most widely studied cross-frequency coupled phenomena in the brain and involves the coupling of distributed, lower frequency theta oscillations and local higher frequency bursts.[30] Thus, cross-frequency PAC is considered to be a physiological marker that links distributed brain regions during

bouts of coherent activity to integrate information across different spatiotemporal scales.[30] Furthermore, previous work has proposed that phasic REM sleep may support cortical-hippocampal dialogue through this theta frequency-based coordination.[31] Phasic REM is characterized by higher theta power and frequency as compared to tonic REM in both the neocortex and hippocampus.[16,17] Thus, we detected putative bouts of phasic REM as periods of elevated theta power (**Figure S2**). We further quantified the inter-peak-intervals of the filtered CA1 theta signal during low and high theta power bouts to determine whether they may correspond to tonic and phasic substages, respectively, and find that high theta power is also associated with higher theta frequency, based on lower inter-peak intervals (**Figures S2A,B**). The rate of REM ripples, as well as chaining of events, was elevated during periods of high theta power (**Figure S2C**), indicating that REM ripples preferentially occur during bouts of putative phasic REM sleep. We restricted further analyses for quantifying gamma and ripple coupling to theta oscillations to these phasic bouts of high theta power. To further validate the coupling of theta, gamma, and ripple oscillations (**Figure 1D**), we quantified PAC between theta phase and gamma to ripple frequency (40-250 Hz) amplitudes (**Figure 2A**). Examining the modulation indices at two discrete frequency bands, gamma (40-100 Hz) and ripple (150-250 Hz), revealed a higher frequency, ripple component that is also modulated by theta phase (**Figures S2D-I**). Additionally, we quantified nesting of gamma and ripple to theta oscillations (Methods) and confirmed the presence of separate gamma and ripple frequency components that are tightly coupled, with gamma events leading ripples (**Figures 2B** and **S2F**,**G**). Furthermore, the phase locking preferences of PFC neurons to these two oscillatory components differ (**Figure 2C**), confirming gamma and ripple separation, and potentially reflecting distinct modes of local ensemble memory related processing. Importantly, we observed elevated CA1-PFC theta coherence during these REM ripples as compared to baseline (**Figure 2D**), suggesting that increased coherence is associated with ripple generation in PFC during REM sleep.

Since we observed short-latency ripple recurrence during REM (**Figures 1F,G**), we reasoned that these ripple “chains” may be functionally different than ripples that occur in isolation. Indeed, previous studies have characterized oscillatory events in multiple brain areas that occur in temporal clusters.[32-35] Importantly, chains of spindle events (termed, “spindle trains”) in NREM sleep have been shown to underlie persistent reactivation of awake patterns and are associated with precise spatiotemporal coupling of sleep oscillations.[33] Similar to this study, we find spindle train events in PFC during NREM sleep (**Figures S3A-D**), supporting the claim that PFC exhibits temporally clustered events during sleep. We identified chains of ripples as events that occur within 200 ms of each other (37.9% of all events). Ripple chains were more prevalent in REM than NREM sleep (**Figure 2E**) and similar to spindle trains, predominantly occurred in doublets (**Figures 2F** and **S3C,E**). REM ripples exhibited higher consistency of phase locking to the theta oscillation as compared to NREM ripples (**Figure 2G**), confirming phase modulation. Furthermore, REM ripple chains were strongly phase modulated by theta in both PFC and CA1 and had similar properties to isolated ripples (**Figures 2H** and **S3H**). The strength of gamma was also elevated during ripple chains and exhibited phasic power fluctuations when coupled with ripples, further demonstrating strong temporal coupling (**Figures 2I** and **S2J**). Corroborating the strong phase locking of chain ripples to theta oscillations in PFC and CA1 (**Figure 2H**), we find that hippocampal-prefrontal coherence is elevated during chain ripples as compared to isolated events (**Figure 2J**), with CA1

leading PFC (**Figure 2K**), highlighting a mechanism through which chains of ripples reflect hippocampal-prefrontal coordination to support REM sleep-mediated memory consolidation.

Differential modulation of PFC neuronal activity during NREM- and REM-sleep prefrontal ripples

Since we observed theta modulated population activity aligned to REM ripples that differed from activity aligned to NREM ripples (**Figures 1H,I**), we next examined PFC responses to determine how activity surrounding these events are organized at the level of single units and ensembles. Similar to population responses, many PFC neurons exhibited oscillatory spiking aligned to REM ripples (**Figure 3A**). Unlike NREM ripples, REM events were associated with a broader distribution of activity peaks, suggesting a more sequential structure of neuronal firing surrounding these events (**Figures 3A,B**). Furthermore, PFC neuronal activity was able to distinguish NREM and REM ripples, indicating differences in content (**Figure 3C**). In line with elevated CA1-PFC theta coherence surrounding REM ripples (**Figure 2C**), we found that a subset of CA1 neurons were modulated by these events (**Figure 3D**), indicating enhanced interregional coactivity, potentially delineating periods of CA1-PFC ensemble reactivation to support memory consolidation. Overall cortical coactivity and assembly strength were reduced during REM ripples relative to NREM events (**Figure 3E**), consistent with activity suppression during ripple chains (**Figures 3F-G**), which can gate selective reactivation of PFC ensembles in REM sleep. Examining population spiking activity, we found that PFC activity was strongly theta-modulated during REM ripple chains, compared to both isolated and NREM events (**Figures 3F** and **S3F-H**), and this phasic population response was largely due to the association with ripple events and not necessarily periods of high theta power (**Figure S3I**). Interestingly, only ripple chains were uniquely associated with a decrease in overall local population activity (**Figures 3F,G** and **S4**), which is in contrast to the strong excitation seen in PFC and CA1 during NREM PFC ripples and SWRs, respectively.[23] Since REM ripples predominantly occur in doublets (**Figure S3E**), sublinear integration may underlie the population suppression during ripple chains and can reflect privileged temporal windows for selective PFC ensemble reactivation and strengthening.

PFC ensemble activity is sequentially organized by REM ripple chains

Since we observed a broader distribution of activity (**Figure 3B**) as well as multiple peaks in population activity during REM ripple chains (**Figure 3F**), we next examined, in more detail, how activity is structured around these events. Previous studies have shown that the refractoriness of certain oscillatory events, such as spindles and SWRs, elicits differential population responses.[32,33,35,36] Thus, we first examined population dynamics based on the temporal separation of REM ripples and found that ripple adjacency determines the similarity of the reactivation content in PFC across ripple events (**Figures 4A,B** and **S4D**). Reactivation similarity as a function of Inter-Ripple-Interval (IRI) was examined using quartile ranges for the intervals between ripples. Quartile 1 had the highest correlation, with the average IRI of this quartile as 114 ms (theta frequency, corresponding to ripple chains), indicating that adjacent ripples events in ripple chains

show a high degree of similarity as compared to adjacent isolated events. Furthermore, rank order analysis on the content of concatenated ripple chains demonstrated a preserved sequential firing of PFC neurons across events (**Figure 4C**), suggesting a process through which ripple chains organize PFC activity in a stereotypic manner that allows for sequential reactivation of distinct assemblies.

To test this sequential reactivation, we next assessed PFC assemblies by time-locking PFC reactivation strength to NREM and REM ripples. Similar to single unit modulation, the timing of PFC assembly reactivation aligned to NREM ripples was largely restricted to 200-500 ms after ripple onset, depending on the ripple type examined (**Figures 4D** and **S4I**). For REM events, only the first ripple within a chain was selected for alignment, since we found that peaks in population activity occur prior to the onset of a ripple chain (**Figure S4E**), possibly facilitated by strong phasic gamma surrounding ripples (**Figures 2I** and **S2J**). We found that unlike NREM ripples, where assembly reactivation is synchronous and consistently highest at the onset of events, PFC assemblies were sequentially organized surrounding REM events, similar to single unit modulation (**Figures 3A,B** and **4D**). This temporal tiling of assembly reactivation aligned to REM ripples manifested in a relatively flat average response, highlighting the differential engagement of PFC assemblies during NREM and REM ripples (**Figure 4E**). To confirm the sequential activity during REM ripples, we quantified the consistency of the assembly reactivation using a cross-validated approach (see Methods). Consistent with the high temporal coordination between chain events and gamma (**Figure 2H**), we found the greatest degree of sequence similarity during REM ripple chains and gamma events compared to shuffled data, confirming the tendency for PFC assemblies to be reactivated in a stereotyped, sequential manner as compared to isolated REM and NREM ripples (**Figures 4F-H** and **S4F-I**).

Differential engagement of PFC REM ripple chains by distinct populations of CA1 neurons

Theta coherence and phase amplitude coupling are two prominent modes of interregional coordination thought to underlie mnemonic processing.[30,37] Since we observed an overall increase in CA1-PFC theta coherence and gamma power during ripple chains (**Figures 2H,I**), as well as sparse modulation of CA1 activity during REM ripples (**Figure 3D)**, we reasoned that there may be specific populations of CA1 neurons that are engaged by these events. Examining CA1-CA1 cofiring during these events, we observed a higher degree of spatial correlation for high cofiring pairs, suggesting reactivation of behaviorally relevant hippocampal assemblies, to support memory consolidation[10] (**Figures 5A,B**). Additionally, the absolute CA1 cofiring, comprising both negative and positive magnitudes of cofiring, was higher during ripple chains, indicating a distinct activity profile compared to isolated ripples (**Figure S5A**). Next, we evaluated interregional activity and observed a bimodal distribution of CA1-PFC cofiring during REM ripples, indicating a subpopulation of CA1 cells that are highly engaged with PFC neurons (**Figure 5C**). Examining low and high cofiring CA1 neurons during REM ripples showed that indeed high cofiring CA1 neurons exhibited elevated activity during chained events as compared to low cofiring CA1 neurons (**Figure 5D**).

Interestingly, we also found a relationship between CA1 reactivation during REM PFC ripple chains and CA1 suppression by NREM PFC ripples. CA1 neurons that exhibited high cofiring with PFC specifically during REM ripple chains were more strongly suppressed during independent NREM PFC ripples, and the degree of suppression was correlated with the strength of REM CA1-PFC cofiring (**Figures 5E** and **S5C,D**), suggesting a role for NREM ripples in tagging of specific CA1 populations for subsequent modification during REM sleep. However, although there was a strong relationship between CA1 suppression during independent PFC ripples and excitation during coordinated SWRs in NREM sleep, as shown in a previous study[23] (**Figures S5C,E**), we did not find correlations between CA1 REM cofiring and SWR reactivation (**Figure S5F**), indicating that these CA1 sub-populations are specifically engaged by PFC ripples, with reactivation during REM and suppression during NREM.

Previous studies have shown that NREM and REM sleep are involved in modifying hippocampal excitability, with a net decrease in firing rates over the course of sleep.[38,39] Interestingly, we observed that these high REM ripple cofiring CA1 neurons differentially shifted their firing rates upward over the course of a sleep session, whereas most of the neuronal population, including low REM ripple cofiring cells, decreased their firing rates (**Figures 5F**, **S5B**, and **S6A-E**), consistent with the role of REM sleep in hippocampal firing rate diversification.[40] This effect was hippocampal specific; there was no differential regulation of PFC firing rates over the course of sleep (**Figure S6F**). Furthermore, the degree of cofiring with PFC during REM ripples predicted CA1 firing rate changes during sleep, and this relationship was absent for NREM PFC ripples (**Figures 5F** and **S6E**). Splitting the population in half based on mean firing rate changes further confirmed this relationship (**Figure 5G**), suggesting a REM specific role of PFC ripples in modifying hippocampal excitability.

The dorsal CA1 pyramidal cell layer can be anatomically segregated into deep and superficial sublayers that are molecularly defined, have differential engagement with hippocampal SWRs and cortical areas,[41-44] and employ complementary spatial codes for effective coding of environments.[45] Notably, deep layer neurons in CA1 preferentially shift their preferred theta phase from run to sleep[13] – a phenomenon that is experience dependent.[46] We therefore investigated whether there were differences in REM ripple recruitment for non-shifting and REM-shifting cells. We categorized REM-shifting neurons as cells that had a difference in phase preference greater than 90°.[13] As expected, there was a subset of CA1 neurons (putative deep layer cells) that shifted theta phase preference and were strongly engaged by SWRs (**Figures S6G-I**), as previously reported.[42] Similar to high cofiring CA1 neurons, these REM-shifting cells had higher coactivity with PFC than non-shifting cells (**Figure 5H**), and there was a significant relationship between ripple chain cofiring and suppression in the REM-shifting neurons, suggesting a population specific modulatory effect (**Figures 5I** and **S6I**). REM-shifting neurons also exhibited strong bursting activity during ripple chains as compared to isolated events and were more strongly phase locked to the PFC theta oscillation surrounding ripple chains (**Figures 5J,K** and **S6K**). Thus, PFC ripples during REM sleep engage a specific population of REM-phase-shifting CA1 neurons, that are suppressed during NREM cortical ripples, but overall show increase in firing rates during sleep, thus potentially increasing or stabilizing excitability to enhance signal-to-noise for efficient expression during future behavior.

Modeling ripple-associated PFC activity during NREM and REM sleep

To gain a better understanding of how a cortical network can exhibit different activity patterns during NREM and REM ripples, we built a simplified network model (**Figure 6A**). 1,600 excitatory pyramidal and 400 inhibitory interneurons were pseudo-randomly connected based on cortical layer 2/3 connectivity probabilities (see **Methods**). Acetylcholine (ACh) concentration is an especially important factor for differentiating NREM and REM sleep states, with strong impacts on cell-spiking properties and network dynamics.[47-49] To incorporate one of the crucial impacts of ACh concentration on cortical neurons, each neuron in the model used a modified Hodgkin-Huxley (HH) formalism with an additional slow potassium (M-type) leak conductance term. During NREM simulations, this slow potassium channel is opened to simulate low ACh concentration, and the channel is closed for REM simulations to simulate high ACh concentration.[50,51] By incorporating this additional conductance, a primary effect of the most abundant muscarinic ACh receptor in the brain (the M1 receptor) is included in the model. *In vivo* and in the model, activation of this potassium leak current alone reduces cell excitability and increases network synchronicity.[52-56] In the model, modulation of this M-type current also changes the excitatory-inhibitory balance of the network, supporting higher average interneuron rates (**Figure S7A**).

We found that by applying a stimulus input to a randomly chosen subset of cells of the network, we could recreate some essential characteristics of network activity patterns during NREM and REM cortical ripples. A brief moderately strong input during NREM, representing input during NREM ripples, was sufficient to induce a larger burst of synchronous spiking in the network, causing a large peak in Multi-Unit Activity (MUA, **Figure 6B,D,** left). In order to recreate the MUA activity surrounding REM PFC ripples, we found that a theta-modulated gaussian input with a similar profile to the theta power observed around PFC REM ripples (representing activity during phasic theta bursts in REM) was able to capture oscillatory and inhibitory features of the MUA (**Figure 6C,D**). We applied stimulus inputs of a variety of peak amplitudes to the network, and found that for temporally brief, discrete stimuli in NREM, stronger stimulation induced greater MUA (**Figure S7D**). Conversely, the strength of theta-oscillating input (and associated theta power as measured in the model's MUA) during REM correlated negatively with the MUA level during stimulation **(Figure 6E**)**.** We found a similar negative relation in the experimental data between theta power surrounding REM ripple times and MUA level, suggesting that increased theta power in PFC is associated with stronger external input.

The cofiring analysis done on experimental spiking data during REM and NREM ripples (**Figure 3E)** was implemented for the spikes of a matched number of randomly chosen model neurons during REM and NREM stimulation periods, showing greater cofiring during NREM similar to the experimental data (**Figure 6F**). In addition, we divided peaks in MUA during REM stimulation periods in the same manner used to separate isolated and chained REM ripples in the data (minimum 200 ms between MUA peaks, **Figure 2**). Similar to the data, we observed greater theta modulation in the MUA surrounding chained peaks compared to isolated peaks, as well as a larger dip in overall MUA (**Figure 6G**), with the difference especially clear in the pyramidal population of the model (**Figure**

S7H). Overall, these results indicate an ability of the model to capture essential features of PFC activity in NREM and REM sleep, and suggest that REM ripples reflect transient periods of elevated theta input to PFC neurons, leading to characteristic activity patterns in the network due to high cholinergic tone.

Stimulation in NREM induces widespread network activation compared to stimulation in REM

Analyzing stimulation periods in the model's NREM and REM states revealed intriguing differences in network activity (**Figure 7A**). While stimulus periods in REM tended to induce only a slight increase in the total fraction of cells spiking at any given time, stimulation in NREM induced a much wider spread of coactivity throughout the network (**Figure 7B**). We showed that the wider spread of coactivity depended on the decreased ACh concentration characterizing the NREM state in our model, and not the difference between REM- and NREM-inputs, because application of the brief NREM stimulus during REM did not produce the NREM level of peak coactivity (**Figure S7G**). Analysis of the percentage of PFC cells spiking in periods surrounding NREM and REM ripple times in the model also showed this increased spread of coactivity in NREM, in agreement with the experimental results (**Figures 3A,E**, **4D-E,** and **7B**). However, it is unclear whether the widespread coactivity in NREM is a result of propagation of spiking due to recurrent excitation, or simply greater efficacy by the stimulus in directly inducing spikes in stimulated neurons during NREM. To investigate this, we analyzed model results by separating neurons within each stimulus event into stimulated and non-stimulated fractions. When stimulating in NREM, a widespread barrage of spiking from stimulated cells was followed by a smaller increase in the percentage of non-stimulated cell firing among both pyramidal and interneuron populations (**Figure 7C**). In contrast, during REM stimuli, the number of active stimulated neurons increased, but the effect on non-stimulated neurons was suppressive (**Figure 7D**). Again, swapping stimulus profiles showed that the cholinergic tone in the model plays a large role in creating this difference, especially as the brief NREM-like stimulus applied during REM produces no increase in percentage of coactive non-stimulated neurons (**Figure S7I-J**). Our results suggest that the ACh level regulates the degree to which inputs can induce widespread synchronous network activity, leading to the distinct activity patterns in NREM and REM. Low ACh concentration and the associated reduced inhibitory tone in NREM leads to a rapid spread of activity to many non-stimulated cells upon transient excitatory input to a subset of cells. Such a result suggests that the level of ACh regulates the fraction of cells in a circuit able to response to a stimulus, accounting for the observation of synchronous bursts of reactivation among a large portion of cells during NREM (low ACh and low inhibition) whereas coactivity is restricted to only smaller subsets of cells in the network during REM (high ACh and high inhibition).

DISCUSSION

One of the key challenges in understanding the role of REM sleep in memory consolidation has been disentangling the interregional neurophysiological processes involved in memory-related processing. Previous studies have primarily focused on the role of theta oscillations in REM sleep as a brain-wide pattern that coordinates activity

across various brain regions,[57] due to their similarity with patterns observed during wakeful behavior. While much attention has been focused on investigating theta oscillations due to their prominence in the hippocampus during REM sleep, the precise dynamics that drive the coordination of multiple brain areas to support systems memory consolidation have been elusive. Furthermore, the prominence of oscillatory phenomena in NREM sleep—including slow oscillations, spindles, cortical ripples, and CA1 SWRs—has enabled systematic dissection of their spatiotemporal dynamics and their relationship to hippocampal-cortical reactivation that supports memory consolidation,[9-12] leaving REM sleep poorly understood in comparison.

Here, we show that phasic theta bursts in PFC during REM coincide with chains of local high-frequency ripple events and elevated gamma power. These chains are associated with increased measures of functional connectivity between PFC and CA1, organize sparse, sequential reactivation in PFC over extended time periods, and recruit a sub-population of CA1 neurons for reactivation that exhibit differential regulation of activity over the course of sleep. This is in contrast to NREM sleep, where PFC ripples are associated with relatively brief, synchronous bursts of local reactivation along with suppression of CA1 activity. Importantly, we also show that CA1 co-activation during REM PFC ripples is related to the CA1 activity suppression seen during NREM PFC ripples, with CA1 neurons that are highly coactive with PFC during REM ripple chains being strongly suppressed during NREM ripples, suggesting a dual sleep-stage role of PFC ripples in regulating excitability in hippocampal circuits. Thus, these results uncover a novel, high-frequency pattern of PFC activity in REM that can potentially bridge the gap between structured PFC and CA1 firing patterns in NREM-REM stages and changes in hippocampal plasticity during sleep.

In contrast to PFC ripples in NREM sleep, which are involved in suppressing CA1 activity as a possible mechanism for tagging specific memory traces for consolidation,[23] here we found that REM cortical ripples engage specific populations of CA1 neurons for reactivation as well as to potentially regulate activity homeostasis. Of particular interest regarding this phenomenon of activity regulation is a recent study examining the differential roles of NREM and REM sleep in reorganization of drifting hippocampal assemblies over the course of sleep.[58] This study focused solely on hippocampal assemblies, and the results are in line with our finding of the potential roles of PFC ripples in NREM and REM sleep. We have previously shown that independent NREM PFC ripples that are dissociated from hippocampal SWRs broadly suppress CA1 activity, and that this suppression is related to the strength of CA1 reactivation during SWRs and CA1 assembly reinstatement during subsequent behavior.[23] This bidirectional modulation of hippocampal representations during PFC and CA1 ripples may underlie assembly reorganization during NREM sleep. Relatedly, we report here that CA1 activity during REM PFC ripples is associated with differential changes in excitability in a subset of hippocampal neurons during sleep, which may, in part, contribute to the stabilization of assemblies in REM sleep and thus drive the sleep-stage dependent reorganization of hippocampal assemblies. We speculate that PFC REM ripple chains enable selective linkages between the sparsely reactivated PFC ensembles in coordination with the subset of co-activated CA1 ensembles. A limitation of our study is the inability to investigate the relationship of the REM reactivation phenomena to learning. Spatial memory tasks in rodents similar to our study have revealed causal links of NREM reactivation driven by CA1 SWRs to learning and memory consolidation[59-62], but reports of REM reactivation

are rare.[63] Investigation of the role of REM reactivation in learning and memory consolidation will need utilization of tasks known to require REM and NREM states, such as inference or emotional memories.[64-67] Future experimental and network modeling studies can investigate how neuromodulatory mechanisms and NREM and REM state-specific cortical activity patterns support learning and memory consolidation.

Cortical high-frequency oscillations (~120-160 Hz) have been reported before, especially in parietal cortex, although they have been variously termed fast gamma or HFOs (high-frequency oscillations),[17,19,20,26] with previous reports of strong coupling with theta oscillations in REM.[26] HFOs have also been reported in parietal cortex and hippocampus during active waking behavior and REM, and it has been argued that HFOs in hippocampus are distinct from hippocampal SWRs.[20] There is, however, no clear distinction between PFC HFOs and ripples, and we used similar ripple detection criterion in both NREM and REM states to identify these cortical high-frequency oscillations, revealing the reported phenomenon of PFC ripple chains. PFC ripples are thus seen both in NREM and REM; in NREM, these occur independently of hippocampal SWRs and are associated with temporally synchronized local PFC reactivation and suppression of hippocampal activity and reactivation,[23] while in REM, they present as PFC ripple chains during theta-modulated activity, associated with sparse, temporally extended local reactivation in the backdrop of suppression, along with co-reactivation of a hippocampal-subpopulation.

External drive can lead to the generation of PFC ripples and synchronized activity in NREM, whereas high acetylcholine (ACh) and high inhibitory tone in REM can lead to local suppression in response to external drive.[68-70]. Notably, a recent study demonstrated that differential cholinergic modulation, together with the sequential architecture of sleep (NREM to REM transition), supports memory consolidation through the complementary shaping of ensemble activity during NREM and REM sleep [51]. We show here that a simple network model that incorporates the effect of differential ACh tone on excitatory and inhibitory neurons in REM vs. NREM states is able to reproduce the observed experimental activity patterns in response to stimulation, akin to phasic theta bursts during REM and isolated, brief inputs in NREM. It is likely that PFC ripples are generated locally and modulated by external inputs. We speculate that theta-modulated input to PFC during REM is driven by hippocampal inputs, but it is also possible that theta is driven by inputs arising from regions other than the hippocampal network, a possibility which will require further experimental investigation.

We observed that isolated REM ripples in PFC were more prevalent than chains, potentially reflecting the need for coordinated activation of distributed circuits to elicit ripple-associated phasic events. One possible mechanism driving this phenomenon could involve ponto-geniculo-occipital (PGO) waves, which are prominent during phasic REM and are known to play a role in modulating hippocampal plasticity during REM sleep.[71] These waves are also coordinated with both SWRs in NREM and theta states in REM,[71,72] suggesting that PGO-associated amplification of hippocampal theta oscillations could drive activity above a certain threshold for ripple generation in PFC. Additionally, ACh may also play a role in altering the threshold for ripple generation in PFC in conjunction with PGO coordination. It has been reported that there is coordinated release of ACh in PFC and dorsal hippocampus, potentially elevating coherence between the two areas.[73] Indeed, a number of studies have shown that ACh boosts theta oscillations.[74]

Furthermore, ACh induces decorrelation in cortical circuits, which improves cortical representations of relevant stimuli,[75] and our finding that REM ripples are associated with an overall decrease in PFC population activity, as well as reactivation strength and cofiring, in contrast to NREM ripples, indicates a role for REM ripples in amplifying local signal to noise to link cortically encoded information with specific populations of hippocampal neurons. Lastly, cholinergic input to the hippocampus also suppresses SWR generation,[76,77] which could facilitate the sparse CA1 reactivation during REM sleep for selective changes in excitability and stabilization of salient representations in coordination with cortical networks for subsequent expression during behavior.

Taken together, these results are aligned with REM sleep's role in memory consolidation and provide a neural basis for the cortical-hippocampal modifications that occur during sleep to support mnemonic processing. The complex interplay between oscillations of varying frequencies revealed here further highlight the importance of segregating sleep into multiple states to uncover how systems memory consolidation can be supported through the multiplexing of distinct phases, both during NREM and REM sleep. The interareal dynamics associated with PFC REM ripples involve both bottom-up and top-down processes operating in precise temporal coordination, with theta-mediated communication leading to PFC ripple-associated reactivation and modifications in hippocampal excitability. This, in conjunction with PFC-mediated suppression of CA1 during NREM sleep, suggests a dual sleep stage processing of mnemonic representations that have implications for understanding the circuit mechanisms underlying systems memory consolidation, and can reveal how neural processes in sleep go awry in disease states.

ACKNOWLEDGEMENTS

This work was supported by the National Institutes of Mental Health (R01MH112661 to SPJ).

AUTHOR CONTRIBUTIONS

J.D.S. and S.P.J. conceived the study. J.D.S. performed the experiments. J.D.S. processed and analyzed the data. M.S. conceptualized the model and P.M. advised on model implementation. J.D.S., M.S., and S.P.J. wrote the manuscript. S.P.J. provided supervision and funding for all aspects of the study.

DECLARATION OF INTERESTS

The authors declare no competing interests.

SUPPLEMENTAL INFORMATION

Document S1. Figures S1–S7 and Table S1

MAIN FIGURES

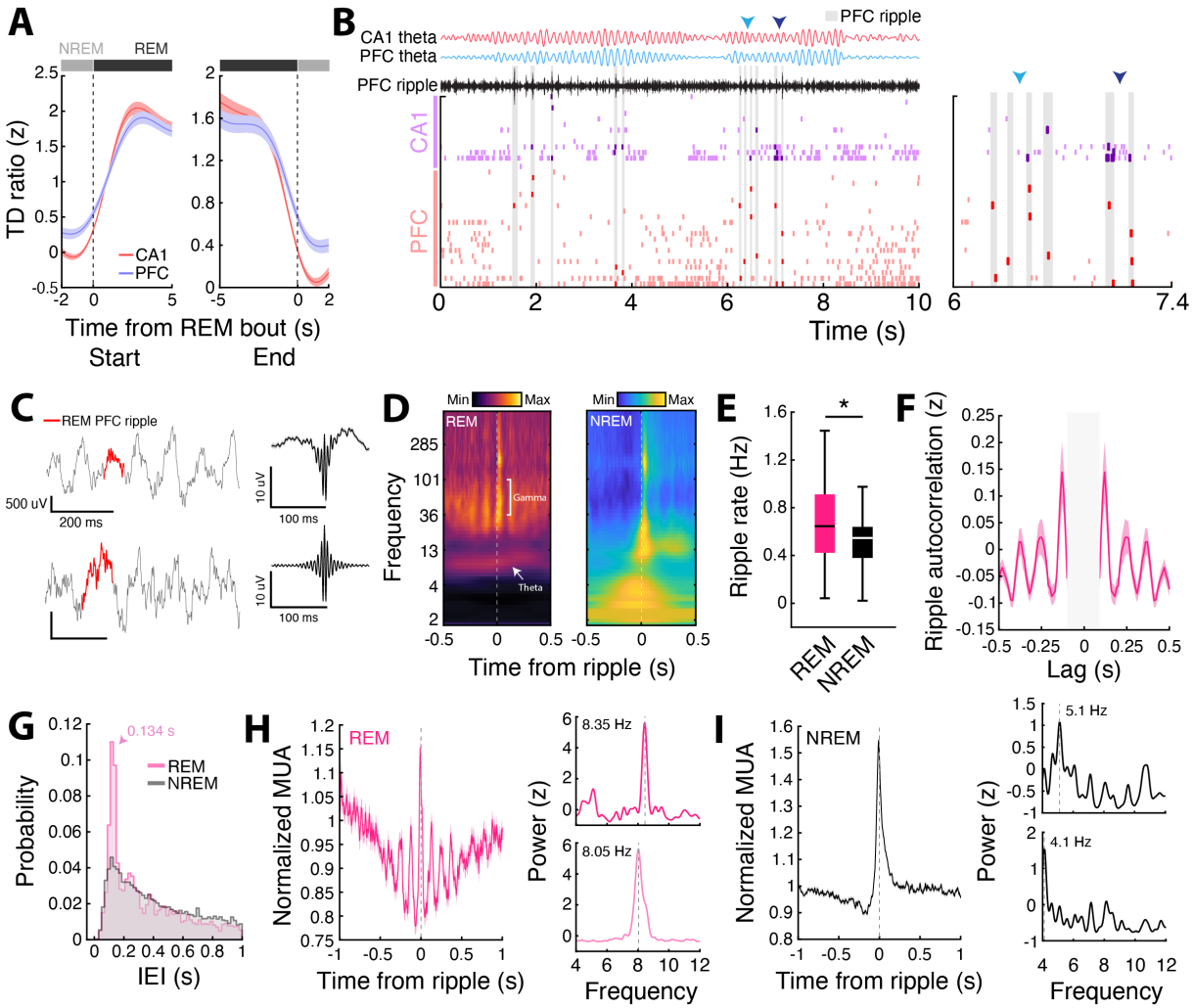

Figure 1. Ripple events in PFC during REM sleep during theta modulated activity.

(**A**) CA1 and PFC theta-delta (TD) ratio time locked to either the start or end of a REM sleep bout. Start and end times were determined using CA1 TD ratio. Note the similar increases and decreases in CA1 and PFC TD ratio surrounding REM bout starts and ends, respectively.

(**B**) Raster plot of CA1 and PFC cells during REM sleep with PFC theta and ripple amplitude plotted above. Gray shaded areas indicate PFC ripples, and arrows denote periods expanded on the right to show single unit spiking during ripple events.

(**C**) (Left) Example PFC ripples during REM sleep. Note the theta frequency fluctuations in the local field potential. (Right) Example grand average PFC ripple waveform (top) and amplitude (bottom) across all events in an example animal.

(**D**) Example PFC ripple triggered spectrogram for REM and NREM ripples. Note the elevated gamma (40-100 Hz) and theta (6-12 Hz) band activity associated with REM ripples, in contrast to the elevated slow oscillation (0.1-4 Hz) and spindle (12-16 Hz) band power in during NREM ripples.

(**E**) PFC ripple rates in REM and NREM sleep (REM = 0.66 ± 0.06, NREM = 0.54 ± 0.05, *p = 0.013, WSR).
(**F**) PFC ripple autocorrelation in REM sleep. Note the peaks in the autocorrelation that repeat approximately every 125 ms.
(**G**) Distribution of inter-event intervals (IEIs) for NREM and REM ripples. Note the prevalence of IEIs less than 200 ms for REM ripples (Mode = 0.134 s). Only IEIs up to 1 s are shown for visualization purposes.
(**H**) (Left) REM ripple aligned multiunit activity in PFC, and (Right) the power spectral density (PSD) calculated for two example animals. The vertical dashed gray lines indicate the peak theta frequency of the population activity fluctuations surrounding ripple events.
(**I**) Same as in (**H**) but for NREM ripples. Top and bottom PSDs are from the animals in (**H**).

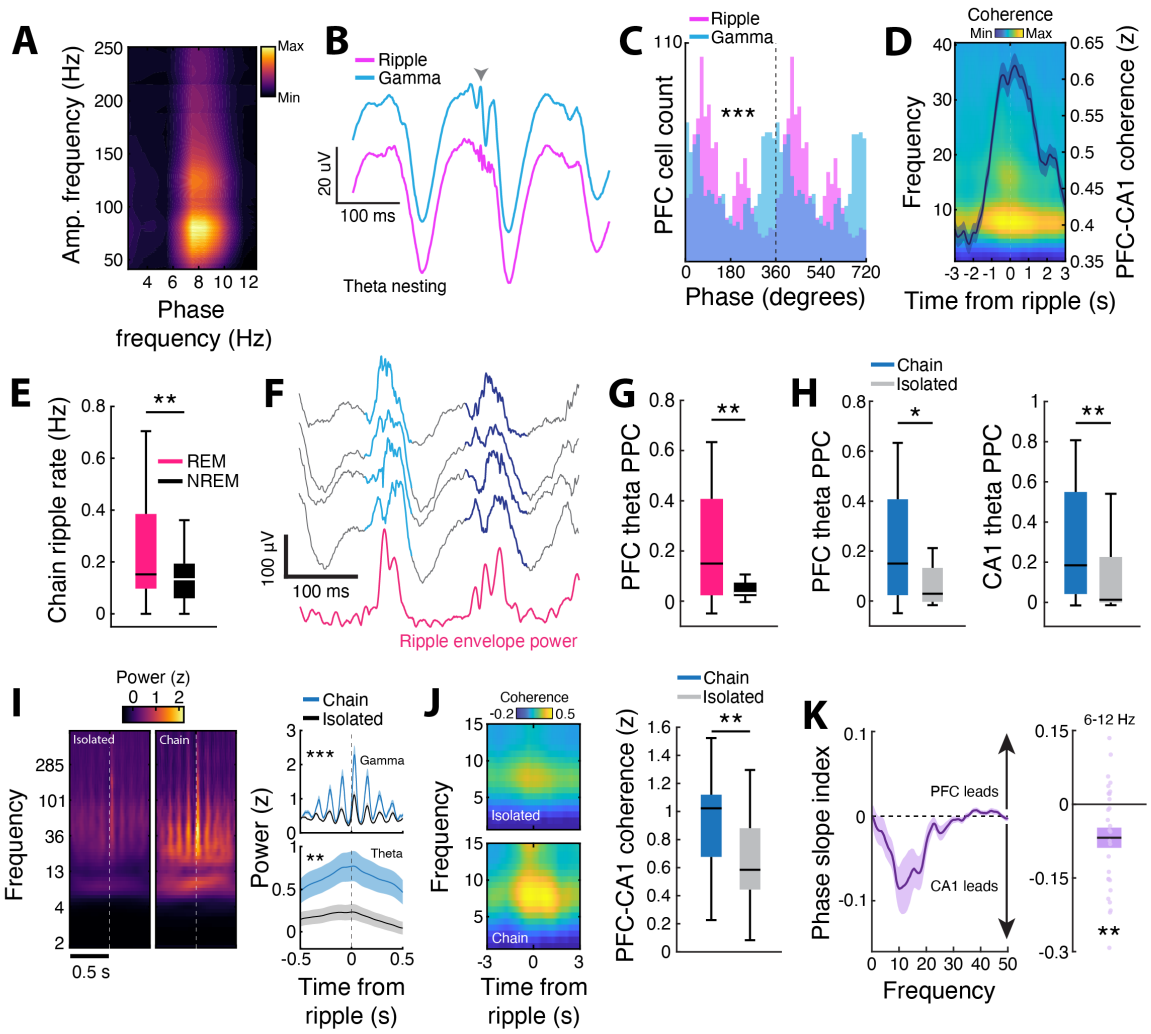

Figure 2. Theta, gamma, ripple coupling underlies distinct REM modulation states in PFC.

(**A**) Averaged modulation across phase-amplitude pair occurrences during high theta power REM periods. The phase of the theta oscillation at a peak frequency of 7-8 Hz strongly modulates the amplitude of higher frequency oscillations.

(**B**) Theta nesting for gamma and ripple frequency oscillations for an example tetrode illustrating coupling of theta, gamma, and ripple oscillations in PFC during REM sleep (see Methods). Briefly, averaged nesting plots were generated by aligning the LFP to the peak power in the preferred theta frequency phase bin for either gamma or ripple oscillations separately.

(**C**) Distribution of preferred phases for PFC cells locked to ripple or gamma events (U^2 = 4.74, ***p = 4.56×10^{-41}, Watson's U^2 test).

(**D**) CA1-PFC theta (6-12 Hz) coherence centered on PFC REM ripples is elevated relative to baseline coherence.

(**E**) Rate of ripple events designated as participating in a chain (<200 ms separation) during NREM and REM sleep (means ± SEM, NREM = 0.15 ± 0.02 Hz, REM = 0.25 ±

0.04 Hz, **p = 0.0054, WSR; boxplots show median as centerline and interquartile range as box).

(**F**) Example REM ripple chain (doublet) plotted across 4 separate tetrodes with the average ripple power plotted below.

(**G**) PFC theta pairwise phase consistency (PPC) of ripple chains in REM vs NREM (REM = 0.22 ± 0.06, NREM = 0.06 ± 0.02, **p = 0.0097, WSR).

(**H**) Ripples chains showed higher PFC (Left) and CA1 (Right) theta PPC compared to isolated ripples (PFC: Chain = 0.22 ± 0.06, Isolated = 0.09 ± 0.04, *p = 0.013, WSR; CA1: Chain = 0.30 ± 0.08, Isolated = 0.14 ± 0.05, **p = 0.0016, WSR).

(**I**) (Left) Chain and isolated ripple triggered spectrograms. (Right) Power in the gamma (top, 40-100 Hz) and theta (bottom, 6-12 Hz) frequency bands for isolated and chained ripples. The average power in each band in the ±500 ms window surrounding ripple onset was used for comparison (Gamma: Chain = 0.72 ± 0.06, Isolated = 0.45 ± 0.03, ***p = 8.12×10^{-7}, WSR; Theta: Chain = 0.60 ± 0.20, Isolated = 0.15 ± 0.11, **p = 0.0021, WSR)

(**J**) (Left) CA1-PFC theta (6-12 Hz) coherence during chained vs isolated events and (Right) quantification of the peak coherence in a ±1 second window from ripple onset (Chain = 0.93 ± 0.08, Isolated = 0.65 ± 0.05, **p = 0.0069, WRS).

(**K**) (Left) Phase slope index (PSI) peaked at theta frequency, indicating a CA1 to PFC directed flow of information during ripple chains. (Right) Quantification of PSI in the theta band (6-12 Hz). Each data point corresponds to the averaged PSI across each electrode pair in an epoch. (PSI = -0.068 ± 0.021, **p = 0.0025, t-test against zero).

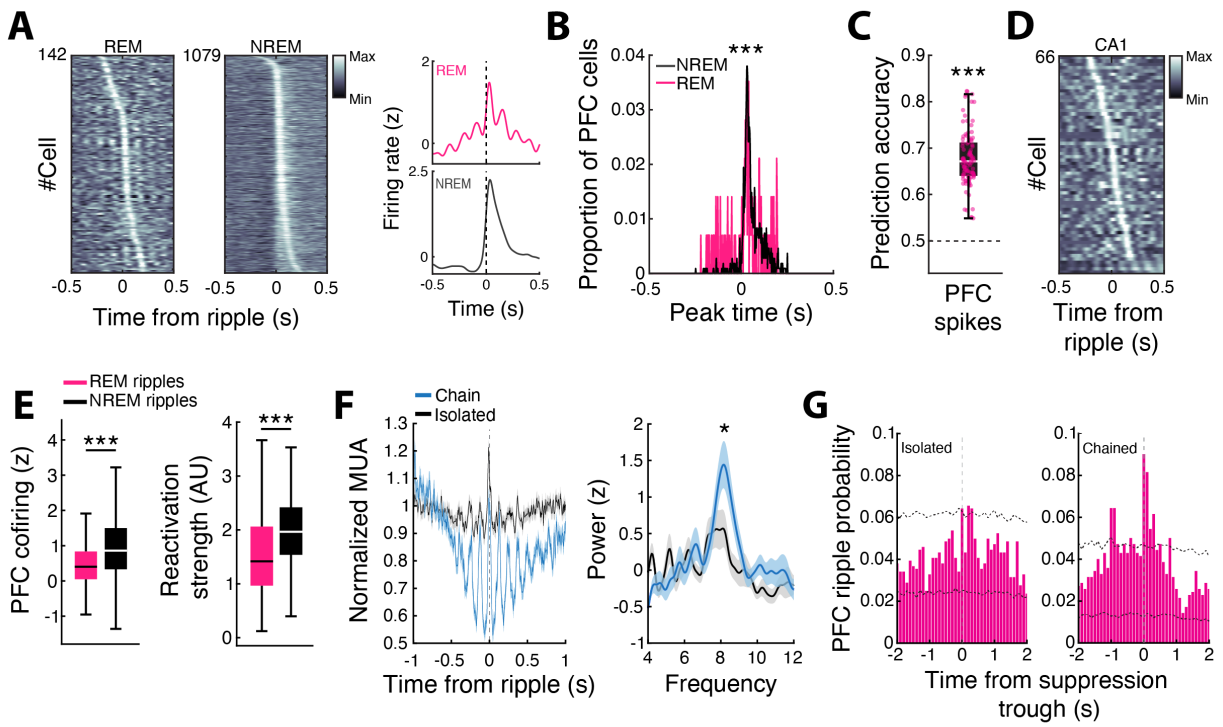

Figure 3. Differential modulation of PFC neuronal activity during NREM- and REM-sleep prefrontal ripples.

(**A**) (Left) PFC neurons that were positively modulated (EXC) during REM and NREM PFC ripple events (REM EXC modulation = 142; NREM EXC modulation = 1079). (Right) Average z-scored peri-event time histograms (PETHs) aligned to ripples.

(**B**) Timing of peak excitation for significantly modulated PFC cells during NREM and REM. Note the broader distribution of peaks during REM sleep (Comparison of peak timing distributions, ***$p = 8.29\times10^{-5}$, WRS).

(**C**) PFC ripple type (NREM vs REM) can be predicted by population spiking activity (PFC data = 0.68 ± 0.01, shuffle = $0.50 \pm 8.00\times10^{-5}$, ***$p = 2.56\times10^{-34}$, WRS).

(**D**) Modulation of putative CA1 pyramidal neurons aligned to PFC REM ripple events (66 EXC neurons, 6.9% of all candidate neurons).

(**E**) PFC cofiring and assembly reactivation strength were overall stronger during NREM ripples (Cofiring: NREM = 0.96 ± 0.03, REM = 0.48 ± 0.03, ***$p = 3.58\times10^{-27}$; Reactivation strength: NREM = 2.01 ± 0.05, REM = 1.56 ± 0.07, ***$p = 6.91\times10^{-16}$, WRS).

(**F**) (Left) PFC multiunit activity aligned to chained vs isolated REM ripple events. (Right) Ripple aligned multiunit PSD illustrating stronger theta modulated spiking activity in PFC during chained events (mean power in the 6-10 Hz band, *$p = 0.029$, WRS).

(**G**) The probability of isolated and chained REM PFC ripples centered on population suppression events detected in REM sleep. Note the strong peak around 0 in the ripple chain distribution, indicating that REM PFC ripple chains are associated with overall decreases in population activity as compared to isolated ripples. The black dotted lines indicate the 99% confidence intervals based on suppression events extracted from shuffled multiunit activity.

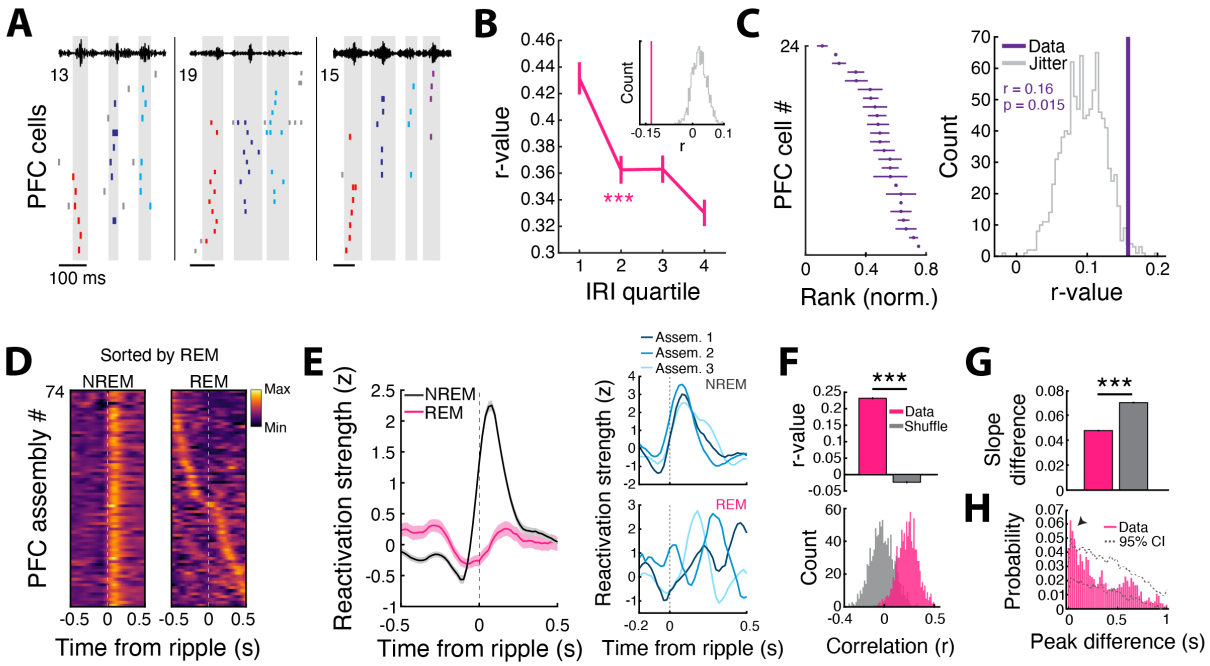

Figure 4. Structured reactivation in PFC during REM ripples.

(**A**) Example rasters during ripple chains. Spikes are color-coded based on the ripple number within the chain during which the cell was active. Note the different cell assemblies active during each ripple within a chain.

(**B**) Correlation of PFC population spiking between adjacent REM ripples and its relationship with inter-ripple intervals (r = -0.13, ***p = 6.00×10^{-8}, Pearson correlation). Note that the average IRI for quartile 1 is 0.114 s, which corresponds to 8-9 Hz during ripple chains. (Inset) The Pearson correlation coefficient compared to a distribution of r values generated from shuffling (n = 1000) ripple identity.

(**C**) Rank-order correlation analysis. (Left) Example rank-order template from an example sleep epoch. Templates were generated by concatenating all ripples in chained events (inter-ripple periods excluded) and averaging the normalized rank across chains. (Right) The mean rank-order correlation compared to a distribution of means generated by jittering (n = 1000) spike times.

(**D**) (Left) PFC assembly reactivation aligned to NREM ripples or (Right) the first ripple of each REM ripple within a chain. The assemblies are sorted based on the average peak reactivation bin within a ±500 ms window surrounding the first ripple in a chain. Note the tiling of assembly peaks aligned to ripple events in REM sleep, which manifests in the relatively flat average response in REM vs. a singular peak of synchronous assembly reactivation in NREM as shown in (**E**).

(**E**) (Left) Averaged ripple triggered reactivation strength during NREM and REM. (Right) Mean reactivation strength of three example assemblies aligned to ripple events in NREM and REM, illustrating the tiling of assembly reactivation relative to events. The example assemblies shown come from the same animal and epoch.

(**F**) Cross-validation of the REM reactivation sequences shown in (**D**), suggesting a consistent structure of reactivation surrounding REM ripple chains. (Bottom) Distributions of r values calculated from the Pearson correlation between peak reactivation bins across

all assemblies for two randomly chosen halves (n = 1000 random splits) of the ripple aligned data (Data = 0.232 $\pm$ 0.003, Shuffle = -0.023 $\pm$ 0.004, ***p = 1.13×10^{-264}, WRS).
(**G**) Differences in slope of the linear fit between the time of peak reactivation (in milliseconds) and assembly identity for two halves of the ripple aligned data (Data = 0.048 $\pm$ 2.21×10^{-4}, Shuffle = 0.070 $\pm$ 2.67×10^{-4}, ***p = 2.31×10^{-302}, WRS).
(**H**) Probability of assembly peak displacement between randomly chosen halves of the ripple aligned data. For each assembly, the absolute difference in peak location was calculated between the two halves. To calculate 95% confidence intervals, assemblies were circularly shuffled, and the peak displacement probabilities were calculated over 1000 random splits of the data. Note the peak at small displacement values, indicating consistency of assembly peak activity across splits.

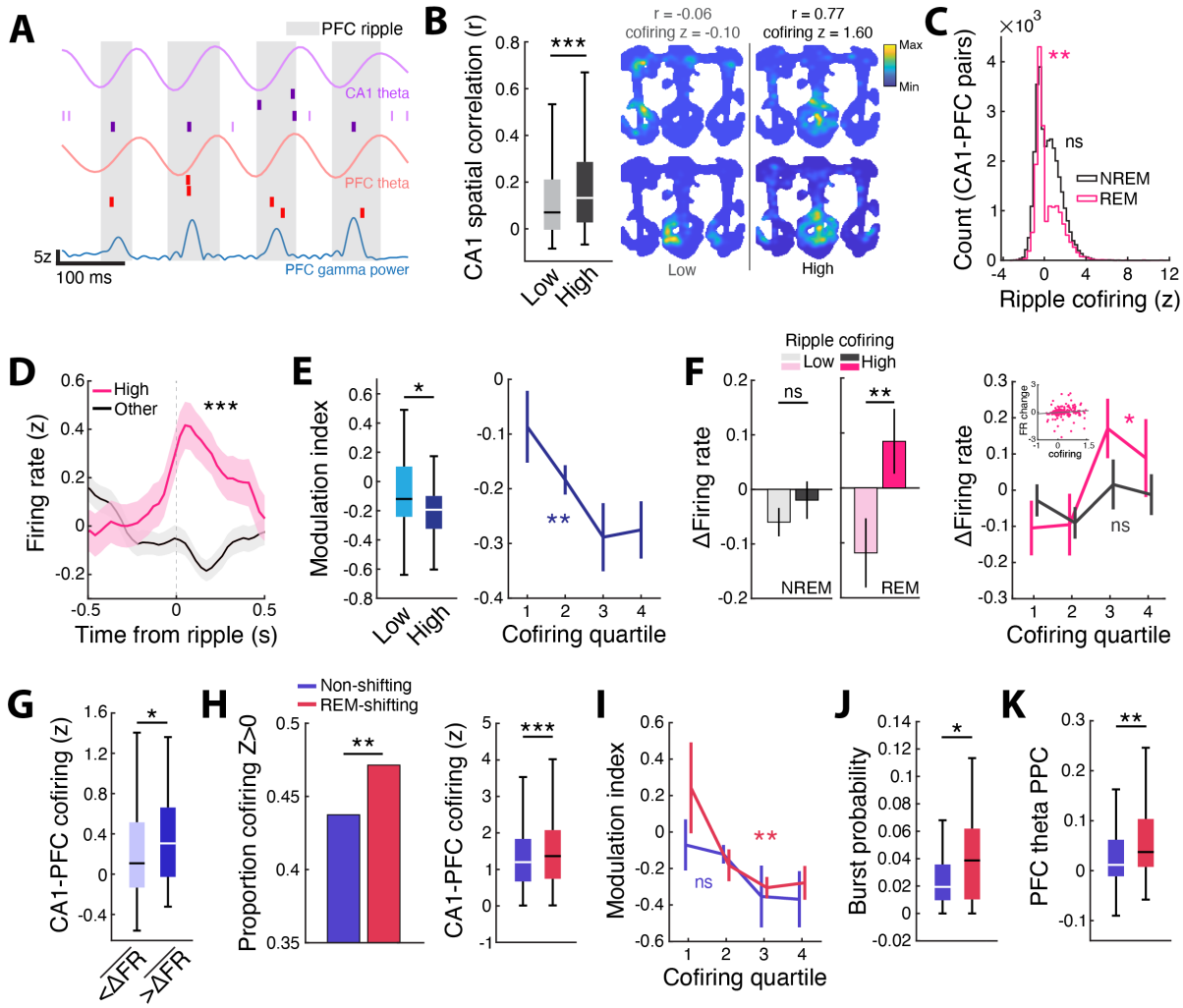

Figure 5. Differential engagement of distinct populations of CA1 neurons during PFC REM ripple chains.

(**A**) Example raster plot of CA1 and PFC cells during a ripple chain event. Only cells that were active during the plotted time window are shown. Note the coherence of theta band activity in CA1 and PFC with elevated PFC gamma power during each ripple event in the chain.

(**B**) (Left) 2D spatial rate map correlation for low and high ripple chain cofiring CA1 pairs (Low cofiring = 0.127 ± 0.001, High cofiring = 0.176 ± 0.004, ***p = 2.37×10^{-45}, WRS). (Right) Rate maps and spatial correlation of example low and high cofiring CA1 pairs.

(**C**) Histograms of CA1-PFC ripple cofiring during CA1-independent NREM PFC ripples and chained REM PFC ripples. Cofiring during REM ripple showed a bimodal distribution indicating separable populations of CA1 neurons based on PFC cofiring. (REM, **p = 0.001; NREM p = 0.23, Hartigan's dip test for bimodality).

(**D**) Firing rate of high cofiring and "other" CA1 cells aligned to ripple chains. Here, 'other' includes low cofiring cells and cells that did not have a cofiring value because at least one of the cells in the pair emitted zero spikes across all events. (Comparison of mean firing rates in the ±100 ms window from ripple onset, ***p = 7.77×10^{-5}, WRS).

(**E**) (Left) High cofiring CA1 neurons exhibited a greater degree of suppression during NREM PFC ripples (Low cofiring = -0.08 ± 0.06, High cofiring = -0.25 ± 0.03, *p = 0.022, WRS). (Right) The cofiring magnitude during ripple chains was correlated with the degree of suppression during NREM PFC ripples (r = -0.23, **p = 0.0045, Pearson correlation).

(**F**) (Left) Changes in CA1 firing rates from the first NREM bout to the last NREM bout within a sleep epoch plotted according to degree of cofiring with PFC (high, > 0; low, < 0), either during CA1-independent NREM or chained REM ripples (Low NREM = -0.06 ± 0.03, High NREM = -0.02 ± 0.03, p = 0.32; Low REM = -0.12 ± 0.063, High REM = 0.085 ± 0.059, **p = 0.0052, WRS). (Right) Firing rate change separated by cofiring quartile. The change in CA1 firing rates over the course of sleep was correlated with PFC cofiring during REM ripples but not NREM ripples (NREM, r = 0.125, p = 0.46; REM, r = 0.169, *p = 0.012, Robust linear regression).

(**G**) CA1-PFC ripple cofiring compared for CA1 neurons with firing rate changes higher or lower than the mean (-0.04 Hz) of the distribution (Higher = 0.34 ± 0.04, Lower = 0.22 ± 0.06, *p = 0.038, WRS). Similar to (**E**), CA1 neurons with positive shifts in firing rate over a sleep epoch had higher PFC cofiring than CA1 neurons with a decrease in rate.

(**H**) (Left) Proportion of CA1-PFC pairs with cofiring greater than 0 during REM ripple chains that contained either non-shifting or REM-shifting CA1 neurons (Non-shifting = 2216/5066 pairs, 43.7%, REM-shifting = 1057/2242 pairs, 47.2%, z = 2.70, **p = 0.0097, Z-test for proportions). (Right) Magnitude of CA1-PFC ripple cofiring (greater than 0) compared for non-shifting and REM-shifting CA1 neurons (Non-shifting = 1.35 ± 0.02, REM-shifting = 1.51 ± 0.03, ***p = 8.30×10^{-5}, WRS).

(**I**) The cofiring magnitude of REM-shifting CA1 neurons was correlated with the degree of suppression during independent NREM PFC ripples (Non-shifting, r = -0.29, p = 0.066, REM-shifting, r = -0.53, **p = 0.0093, Pearson correlation).

(**J**) Burst probability of non-shifting and REM-shifting CA1 neurons during REM ripple chains (Non-shifting = 0.028 ± 0.006, REM-shifting = 0.059 ± 0.017, *p = 0.022, WRS).

(**K**) REM-shifting CA1 neurons showed higher PPC, indicating stronger phase locking to the PFC theta oscillation surrounding ripple chains (Non-shifting = 0.032 ± 0.006, REM-shifting = 0.064 ± 0.011, **p = 0.0026, WRS). Only periods surrounding REM ripple chains were used to evaluate phase locking strength of CA1 neurons.

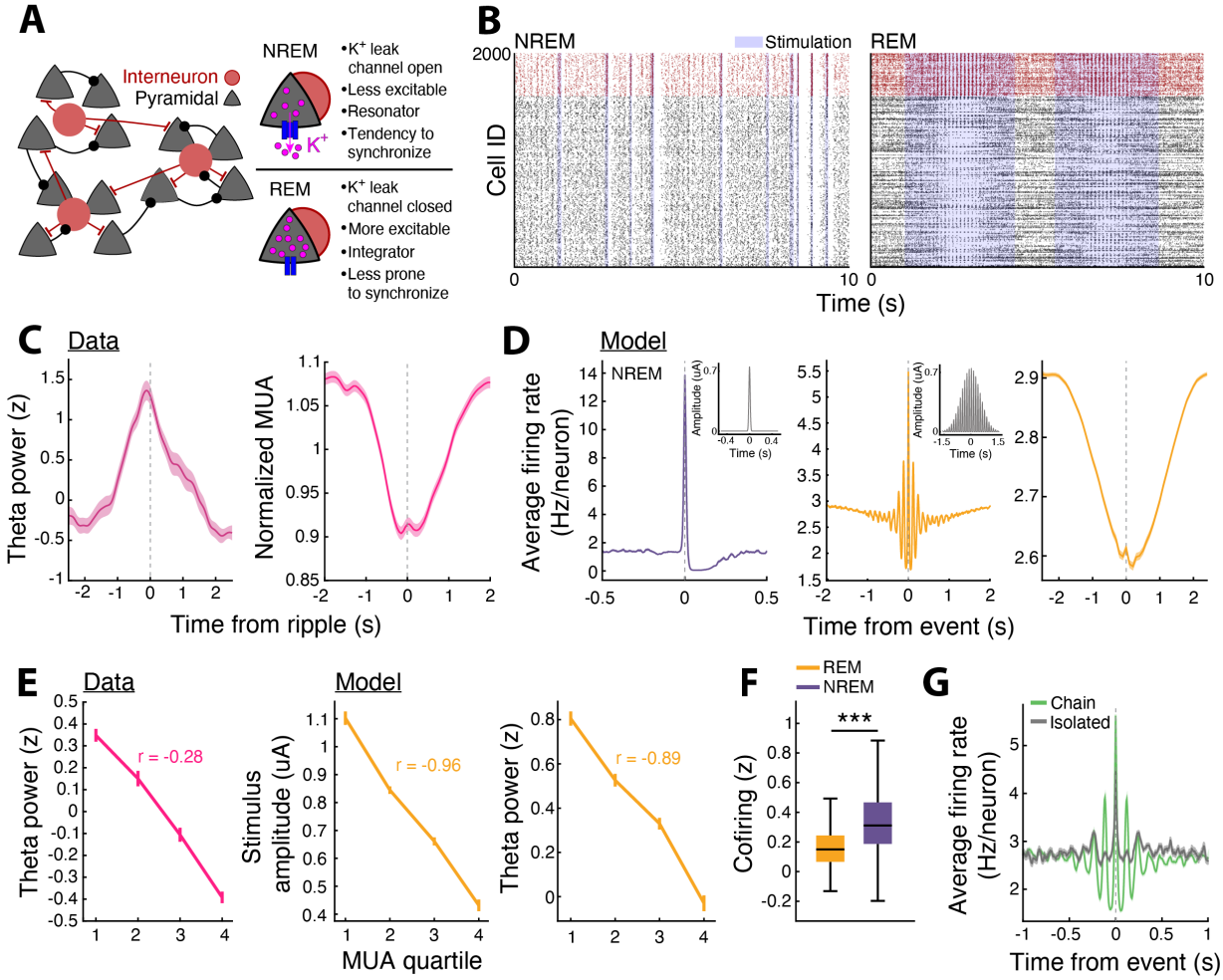

Figure 6. A simple network model incorporating acetylcholine recreates REM results.

(**A**) Model schematic. Network of Hodgkin-Huxley (HH) pyramidal and interneurons with an added slow potassium leak conductance. This channel is open in NREM, introducing an adaptation current that lowers cell excitability and bestows resonator properties to all neurons, altering their phase response curves such that connected cells are better able to synchronize spiking. In REM the channel is closed to simulate high ACh concentration, eliminating the adaptation current.

(**B**) Example raster plots of network activity in NREM and REM. Spikes from 400 interneurons shown in red, spikes from 1600 pyramidal neurons shown in black. Shaded regions indicate periods of applied input current (see **Methods**).

(**C**) Experimental data. (Left) Z-scored theta power surrounding REM PFC ripples shows an average 3 second increase in theta power. (Right) Normalized MUA aligned to REM PFC ripples using 100 ms bins shows suppression.

(**D**) Modeling MUA results. (Left) NREM average network firing rate aligned to MUA peaks during stimulus periods, with inset depicting the average stimulus profile. (Center) same as (Left), but for REM. (Right) REM 100 ms binned firing rate aligned to MUA peaks within stimulus periods (i.e., a smoothened version of the Center panel) shows suppression, similar to experimental data.

(**E**) (Left) Experimental data showing the negative correlation between peak theta power during REM ripples and average MUA during phasic REM sleep. (Center) Peak amplitude of applied stimulus vs. average MUA quartiles during stimulus period in the model. (Right) Same as (Center), but for z-score of average theta power (measured from network MUA) during stimulus period.

(**F**) Z-scored cofiring within MUA peaks in stimulus periods in the model. REM peak duration 37 ± 9 ms (mean ± std), NREM peak duration 35 ± 9 ms.

(**G**) Average firing rate surrounding MUA peaks within stimulus periods in the model split between isolated and chained MUA peaks. Isolated peaks defined as having no other peak within a 200 ms.

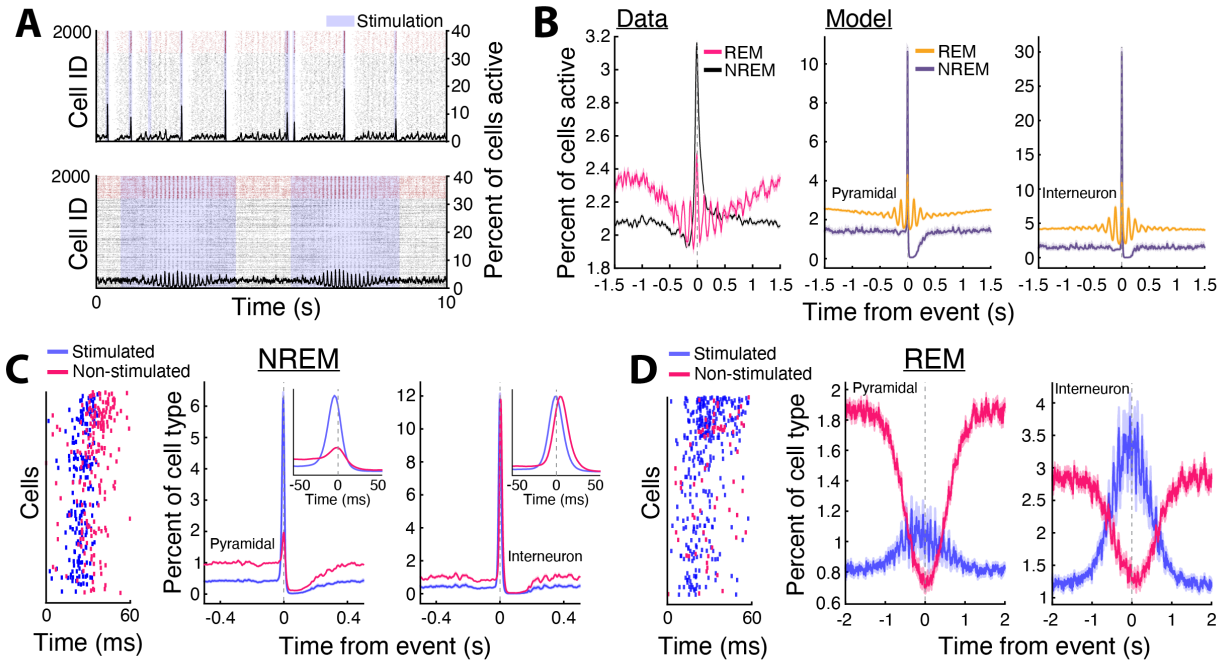

Figure 7. Stimulation in NREM induces widespread coactivity compared to stimulation in REM.

(**A**) Model raster plots during example NREM (Top) and REM (Bottom) periods with black trace indicating the percent of all pyramidal cells with at least one spike in 10 ms bins.
(**B**) The same percent active measure (not distinguishing by cell type) calculated on experimental data aligned to NREM and REM ripples (Left), and in the model aligned to MUA peaks in NREM and REM as a fraction of all pyramidal neurons (Center). Similar plot for all interneurons in the model (Right).
(**C**) Model NREM activity split by cells directly receiving stimulus input (blue) and receiving no external stimulus (pink). Raster of a single example population burst due to stimulation in NREM (Left). Percent of cells with at least one spike in 10 ms bins (as a percent of all pyramidal cells in the network) aligned to stimulus midpoints. The time of peak input amplitude (Center). Similar plot for interneurons (Right).
(**D**) Same as (**C**), but for REM, for a single stimulation event. Note that non-stimulated cell population (pink) comprise a greater percent of total active neurons outside stimulation times (average stimulation time of 3 sec centered at time of event), as there are more neurons in the non-stimulated group (only 30% of neurons are stimulated per stimulus event).

RESOURCES AVAILABILITY

Materials availability

This study did not generate any new unique reagents.

Data and code availability

Data underlying these results will be uploaded in the NWB (Neurodata Without Borders) format to DANDI (ID#TBD) upon acceptance. Code to replicate these results will be available on our lab GitHub (TBD) upon acceptance.

EXPERIMENTAL MODEL AND SUBJECT DETAILS

All experimental procedures were approved by the Institutional Animal Care and Use Committee at Brandeis University and conformed to US National Institutes of Health guidelines. Ten adult male Long-Evans rats (450-600 g, 4-6 months; RRID: RGD_2308852) were used in this study. Animals were individually housed and kept on a 12-hr regular light/dark cycle.

METHOD DETAILS

Behavior

Ten animals were trained on a novel W-maze in a single day, as previously described.[78] Briefly, during the experimental day, all animals ran eight 15-20 minute behavioral sessions on a W-maze interleaved with nine 20-40 minute rest sessions in a sleep box. Reward (evaporated milk) was automatically delivered at each of the 3 reward wells upon completion of a correct trajectory. At the end of a behavioral session, animals were transferred to an opaque sleep box to rest.

Surgical implant and electrophysiology

Surgical implantation procedures were as previously described.[78] Animals (n = 10) were implanted with a microdrive array containing 30-64 independently moveable tetrodes targeting right dorsal hippocampal region CA1 (-3.6 mm AP and 2.2 mm ML) and right PFC (+3.0 mm AP and 0.7 mm ML). For 64 tetrode recordings (n = 1 animal), CA1 and PFC were targeted bilaterally. On the days following surgery, hippocampal tetrodes were gradually advanced to the desired depths using characteristic EEG patterns (sharp wave polarity, theta modulation) and neural firing patterns as previously described.[78] A CA1 tetrode in corpus callosum served as hippocampal reference, and another tetrode in overlying cortical regions with no spiking signal served as prefrontal reference. A ground (GND) screw installed in the skull overlying cerebellum also served as a reference. All spiking activity, gamma, and ripple-filtered LFPs (gamma: 40-100 Hz; ripple: 150-250 Hz; see below) were recorded relative to a local reference tetrode. For detection of slower frequency components (i.e., theta and delta), LFP was recorded with respect to the GND screw. Electrodes were not moved at least 4 hours before and during the recording day.

Data were collected using a SpikeGadgets data acquisition system (SpikeGadgets LLC). Spike data were sampled at 30 kHz and bandpass filtered between 600 Hz and 6 kHz. LFPs were sampled at 1.5 kHz and bandpass filtered between 0.1 Hz and 400 Hz. The

animal's position and running speed were recorded with an overhead color CCD camera (30 fps) and tracked by color LEDs affixed to the headstage.

Histological verification of recording sites

At the completion of each experiment, electrolytic lesions were made by sending current (30 uA) down 3 electrodes per tetrode for 3-4 seconds each. 24 hours later, animals were sacrificed by intraperitoneal injection of Euthasol and subsequent intracardial perfusion with 0.9% saline followed by 4% formaldehyde. The skull, with the attached drive, was submerged in 4% formaldehyde for 24 hours before tetrode retraction and brain extraction. Brains were stored in a 4% formaldehyde and 30% sucrose solution for at least 1 week before slicing with a freezing microtome (Leica) at 50 uM. Slices were Nissl stained and imaged at 4x on a brightfield microscope (Keyence) and stitched together to generate composite images for lesion localization.

Spike sorting

Single units were sorted using a custom manual clustering program (MatClust, M. P. Karlsson) and were distinguished based on spike width, peak and trough amplitude, and principal components. Cluster quality was measured using isolation distance,[79] and only well isolated neurons were included for analysis.

Sleep state identification

To detect bouts of NREM and REM sleep, animals' head speed and CA1 LFPs were used as previously described.[13,14] During sleep box sessions, times of awake activity and immobility were defined as periods where head speed was greater or less than 4 cm/s, respectively. Candidate NREM sleep bouts were identified as periods where head speed remained <4 cm/s after an immobility period of at least 60 s. NREM and REM sleep were further identified and separated by using a theta to delta ratio metric. Briefly, CA1 LFP (referenced to GND) for each tetrode was bandpass filtered (6-12 Hz for theta; 1-4 Hz for delta) and averaged, and the ratio of theta to delta (TD ratio) power was calculated. Periods that exceeded a set threshold (mean + 1 SD) for >10 s were categorized as REM bouts within candidate NREM bouts. Additionally, candidate REM bouts were visually inspected to further confirm the transition into REM sleep. For comparison of velocity and TD ratio, the average velocity and TD ratio in each epoch for NREM and REM sleep were computed and compared. Additionally, only epochs with at least 30 s of REM sleep were included for analysis.

Intracranial electromyogram (EMG)

To estimate EMG from the neck, jaw, and face muscles from intracranial LFP signals, a previously established method was used.[80,81] Briefly, we extracted the 300-600 Hz filtered signal (Butterworth filter at 300 – 600 Hz; filter shoulders from 275 – 625 Hz) and calculated the pairwise Pearson correlations in each 500 ms bin between pairs of electrodes during the entire sleep epoch. Since we used tetrode recordings and cannot determine the exact separation of electrode sites, we elected to calculate the correlations between the reference tetrode in corpus callosum and CA1 ripple detection tetrodes within the dorsal CA1 pyramidal cell layer (~500 μm separation between corpus callosum and the dorsal CA1 pyramidal cell layer), thus maximizing the separation between the electrode sites. Previous studies have used electrode channels on probes at least two shanks apart (~400 μm). The average of all reference/CA1 layer tetrode pairs was

calculated and compared for wake and REM sleep. For the distributions of intracranial EMG values in **Figure S1D**, each 500 ms bin correlation value was reported, and for the comparison between wake and REM sleep, the averages during each wake and REM bout were calculated and compared. A strong relationship between intramuscular EMG and intracranial EMG has been reported.[80]

LFP event detection

PFC ripple detection: Ripple events were detected during immobility periods (<4 cm/s) as previously described.[14] Tetrodes with recorded cells in CA1 and PFC were used as candidate electrodes for event detection as well as downstream LFP analysis. Each LFP from candidate electrodes were bandpass filtered in the ripple band (150-250 Hz), and the envelope power was calculated using a Hilbert transform and subsequently smoothed with a Gaussian kernel ($\sigma = 6$). Ripple events were detected as contiguous periods where the ripple power exceeded 3 SD of the mean on at least one tetrode. Events were further refined as periods around the detected event that remained above the mean (start and end times). The amplitude of each ripple event was reported as the number of SD above the mean.[28] To estimate the frequency of each ripple event, the power in each frequency bin was calculated around each ripple event (±500 ms) using multi-taper time-frequency analysis (Chronux toolbox; http://chronux.org/)[82] and was z-scored relative to a baseline spectrogram. The frequency of each event was defined as the frequency with the highest power in the ripple band (100-250 Hz) between the start and end time of each event.[83] Furthermore, ripple chains were defined as 2 or more ripple events that occurred <200 ms apart. Average amplitude plots for each animal were generated by aligning the peaks of each event and averaging.

PFC gamma detection: Bouts of high gamma power were detected as above after bandpass filtering in the gamma band (40-100 Hz).

High theta power detection: Each LFP from candidate PFC tetrodes were used to delineate periods of high theta power during REM sleep. LFPs were bandpass filtered with a theta band filter (6-12 Hz), the envelope power was calculated using a Hilbert transform, averaged across tetrodes, and periods that exceeded 4 SD of the mean during REM sleep were designated as bouts of high theta power. Only high-power periods exceeding 900 ms were included as high theta power periods.

PFC spindle detection: Spindle events were detected as previously described.[33] The mean LFP across all candidate PFC electrodes was calculated and the resulting signal was bandpass filtered between 10-16 Hz with a zero-phase shifted, third-order Butterworth filter. The envelope power was calculated using a Hilbert transform and subsequently smoothed with a Gaussian kernel ($\alpha = 2.5$). Events that exceeded 2.5 SD of the mean were extracted, and events separated by <300 ms were concatenated. Spindle events were restricted to NREM sleep before analysis. Spindle trains were defined as 2 or more spindle events that occurred ≤2.78 s apart as previously established.[33]

Spectral analysis

Wavelet spectral analyses were utilized to calculate the ripple aligned power spectra in PFC (2–350 Hz, Morlet wavelets). For each epoch, the PFC tetrode with the greatest number of detected PFC ripples was used. The power at each level of the wavelet transform was calculated around each ripple event (±500 ms) and was z-scored relative to a baseline spectrogram calculated for the entire epoch. For each animal, spectrograms from all candidate sleep epochs were averaged.

Event autocorrelation

To calculate the autocorrelation of ripples to assess the structure of event occurrence, identical event time vectors were lagged (max time lag 1 second, 10 ms time bins), and the correlations were calculated. The results were smoothed with a Gaussian kernel (σ = 3) and averaged across all animals and epochs. Similarly, the cross-correlation between gamma and ripple time vectors was calculated by using the gamma times as the reference vector. Thus, positive and negative lag values indicate that the ripples tended to occur before and after gamma events, respectively.

Event aligned multi-unit activity

To characterize population activity aligned to LFP events, spike trains of each neuron were binned into 5 ms time windows. Multi-unit activity was aligned to PFC ripple and gamma events and was normalized by the mean population firing rate during either NREM or REM sleep, depending on the events assessed. Subsequently, the power spectral density of the ripple aligned multi-unit activity was assessed (frequency limits, 2-12 Hz; MATLAB, *pwelch*).

Control for periods of high theta power

To determine whether theta modulated population activity in PFC can be largely explained by periods of high theta power, instead of association with ripple events, we extracted surrogate timestamps to align PFC activity to. Briefly, for each epoch, the preferred theta phase bin of ripple events was calculated from the PFC tetrode with the highest average theta power and used to randomly select surrogate times to align PFC multiunit activity to. Each preferred phase bin at least 250 ms away from a detected ripple was considered a candidate event. Then, times were randomly chosen, and the number of events selected matched the number of ripple events in that epoch. Theta power at each surrogate time point as well as ripple event was extracted and z-scored to control for any inter-animal variability in theta power. Lastly, the event aligned multiunit activity was split into quartiles based on theta power and compared.

Theta inter-peak intervals during bouts of high and low theta power

Since it has been previously shown that tonic and phasic substages of REM sleep can be segregated based on CA1 theta frequency,[13] we calculated the inter-peak intervals of the theta oscillation to determine whether bouts of low and high theta power may correspond to tonic and phasic substages, respectively. We bandpass filtered and averaged the LFPs from candidate CA1 tetrodes between 5-12 Hz, and the peaks were extracted by detecting positive-to-negative zero crossings of the derivative of the filtered, averaged signal. Lastly, the inter-peak intervals were calculated within low and high theta power periods for each epoch and compared. Note that we defined low and high theta periods

based on PFC electrodes, whereas we calculated inter-peak intervals based on CA1 electrodes.

Cross-frequency phase-amplitude coupling

Phase-amplitude coupling was assessed for a range of frequency combinations using a previously established approach.[84] Since the rate of REM ripples was highest during bouts of high theta power, we focused on these periods for assessing phase-amplitude coupling. For each epoch, the tetrode with the highest ripple power was chosen, and an averaged comodulogram was generated across all animals and epochs for the phase and amplitude frequency ranges from 2-12 Hz and 40-250 Hz, respectively.

Comodulogram: Briefly, the phases were extracted from the Hilbert transform of the raw LFP of the candidate electrode and binned into 18 bins (intervals of 20°), and the envelope power of the amplitude modulated frequency band was calculated by taking the absolute value of the Hilbert transform. Then, the amplitude of each frequency from 40-250 Hz was calculated in each phase bin from 2-12 Hz and visualized.

Modulation index: To quantify the depth of amplitude modulation by the phase frequencies, gamma (40-100 Hz) and ripple (150-250 Hz) signals were separately processed, and the mean gamma or ripple amplitude in each phase bin was calculated. The resulting values were used to calculate the modulation index,[84] which specifies the strength of phase modulation. Additionally, the phase bin with the maximum amplitude was reported as the preferred phase. For comparison, the phase and amplitude vectors were circularly shifted independently, and the modulation index was calculated.

Theta nesting

To further investigate the coupling of theta, gamma, and ripples, in PFC during REM sleep, we examined theta nesting[85,86] in two different frequency bands (40-100 Hz for gamma and 150-250 Hz for ripple) relative to the theta oscillation. Since we are evaluating the gamma and ripple coupling specifically during these transient ripple events, we restricted our analysis to high theta periods since the rate of REM ripples was highest during these REM bouts (**Figure S2C**). For each PFC electrode, the theta phase bin for which gamma power was maximal was identified. Then, each instance of this phase bin during high theta periods in REM sleep was detected and the index of the highest gamma power within each preferred phase bin was identified. Only electrodes where there were at least 20 instances of the preferred phase were included. Lastly, the averaged waveform was calculated by averaging the unfiltered LFP centered on every instance of maximal gamma power in the preferred bin. The above procedure was performed separately for ripple band activity. For comparison between the frequency of averaged gamma and ripple waveforms and the preferred phase of theta coupling, electrodes that exhibited at least 5 local maxima within a 100 ms window surrounding the preferred phase were analyzed.

To further validate coupling of gamma and ripple to theta, surrogate waveforms were generated by randomly selecting a different phase bin for each theta cycle for alignment of gamma or ripple power. Then, peak-to-trough amplitudes were calculated from the average waveform within the 100 ms window centered on peak power, averaged, and

compared between the preferred phase bin aligned data and the random phase bin surrogate.

Ripple aligned modulation

Single unit ripple modulation in CA1 or PFC was calculated as previously described.[23,87] This analysis was restricted to neurons that fired >50 spikes cumulatively across all peri-ripple windows (±2 s). For each candidate neuron, an averaged ripple-triggered (CA1 or PFC ripple) time histogram (ripple-PSTH) was calculated. For comparison, 1000 shuffled ripple-PSTHs were generated by circularly shifting the spikes around each ripple event by a random amount. To determine whether a neuron was significantly modulated, the squared difference between the real ripple-PSTH and the shuffled data in the -200 to +200 ms window (0 to +200 ms window for SWRs) after ripple onset was calculated. If this real value exceeded 95% of the shuffled values, the neuron was categorized as significantly modulated. The modulation index for each cell was given by calculating the average difference between the activity in the response window and a background window -600 to -200 ms from ripple onset. Furthermore, excited (EXC) and inhibited (INH) neurons were separated based on whether the modulation in ripple response window was positive (EXC) or negative (INH). Modulation timing distributions for EXC PFC neurons during NREM and REM PFC ripples were compared by binning (2 ms bins) the peak responses within the modulation window.

Ripple type prediction

Ripple type (NREM or REM) in PFC was predicted by fitting a linear model (MATLAB, *fitclinear*) to PFC spike count data. Since the NREM events largely outnumbered the REM events, the event counts were equalized prior to training by randomly excluding a subset of NREM events. The binary decoders were built using 10-fold cross validation, and prediction accuracy was assessed by comparing performance against models constructed with randomly permuted spike matrices (n = 1000). To account for the excluded events, this entire process was repeated 10 times for each animal and epoch.

Theta coherence

Coherence between pairs of CA1 and PFC tetrodes was calculated during REM sleep periods centered on REM ripples, and each frequency was normalized by the mean and SD of the baseline coherogram computed across the entire epoch. Coherograms were averaged over CA1-PFC tetrode pairs. For quantification and comparison, coherence was measured as the peak coherence between 6-12 Hz in a ±1 s window around ripple events. For visualization of coherograms, the averaged coherograms across all animals and epochs were smoothed with a 2D Gaussian kernel ($\sigma = 4$). All coherence-based analyses were conducted using the Chronux toolbox.[82] Only epochs with at least 20 events were included for quantification of peak coherence.

Phase slope index

Since we observed elevated theta coherence between CA1 and PFC during chained events, we assessed the directionality of information flow at different frequency bands (0-50 Hz) centered on these events (±1 s) using the phase slope index (PSI),[88] which was calculated with the FieldTrip analysis toolbox.[89] Briefly, for each epoch, the PSI was calculated and averaged across each candidate CA1-PFC tetrode pair. Here, positive PSI

values indicate that PFC theta leads CA1, while negative values indicate that CA1 leads PFC. Then the distribution of mean PSI values within 6-12 Hz was tested against 0 with a t-test. Only epochs with at least 5 chained events were included for analysis.

Phase-locking

Phase-locking during active behavior on the W-Track and during REM sleep was quantified using previously developed methods.[90] The CA1 or PFC tetrode with the greatest ripple power was filtered in the theta (6-12 Hz), gamma (40-100 Hz), or ripple (150-250 Hz) range and was used to extract phase information. For ripple and gamma phase locking of PFC cells, each spike that occurred across all extracted events were assigned a phase, and the distributions of the peak phases of all cells were compared between gamma and ripple. During run sessions (for 'REM theta phase shifting' analysis below), spikes were restricted to CA1 theta periods where the animals' speed was >5 cm/s and were assigned a phase between 0-360°. Only neurons with at least 10 spikes during theta periods were included in this analysis. The Rayleigh test was used to determine whether the phase distribution of each cell deviated from circular uniformity ($p < 0.05$ criterion). To test for phase preference differences, the distributions were compared using a nonparametric Watson's U^2 test. Subsequently, for each theta modulated cell, phase locking strength to the theta oscillation was measured using pairwise phase consistency (PPC).[91] PPC was calculated by taking the dot product of the angular difference between each pair of phase values then averaging. Similar procedures were performed to determine the ripple and gamma phase preference of PFC cells.

Additionally, PPC was used to assess the strength of theta phase locking of ripple events in REM or NREM sleep. Only epochs with at least 20 events of each type were included for analysis.

REM theta phase shifting

To assess shifts in the preferred CA1 theta phase of CA1 neurons between run sessions and REM sleep, the above procedure was performed, and only neurons that exhibited significant phase-locking during both run and REM sleep were included for analysis. Neurons that had a phase shift of >90° from the preceding run session to the subsequent REM sleep epoch were categorized as REM-shifting.

Single unit PFC ripple bursting

To determine ripple burst probability for each cell, the number of ripples where burst spikes were detected (at least 2 spikes <6 ms apart[92]) was divided by the total number of ripple events.

Detection of population suppression

To validate the suppression of PFC multiunit activity surrounding REM PFC ripples, periods of decreased PFC activity were separately extracted, and the probability of REM ripples surrounding these events was calculated. First, multiunit activity was binned (5 ms bins), normalized by the average activity during REM sleep, and smoothed with a Gaussian kernel ($\sigma = 3$). The population activity was then z-scored, and periods that fell below 0 for 300-500 ms were extracted as population suppression events. Lastly, the probability of ripple occurrence surrounding these events was calculated in 100 ms bins.

To obtain the 99 percent confidence intervals, suppression events were extracted from shuffled multi-unit data. Briefly, each cells' spike count was circularly shifted independently, and events were detected. A total of 1000 shuffles were performed, and the probability of ripple occurrence surrounding these events was calculated for each shuffle.

Relationship between inter-ripple interval (IRI) and content of adjacent ripples

To assess whether there was a relationship between IRI and population spike content between ripple events, the spiking activity of PFC neurons during ripples was represented as ones and zeros for either active or inactive during all events. The Pearson correlation between population activity vectors of two adjacent ripples was calculated, and the IRI was given by calculating the temporal difference between the centers of the ripple events. Then, the relationship between spike content and IRI was assessed using the Pearson correlation coefficient. To validate this relationship, we employed two other methods for quantifying similarity of activity across two events, the Jaccard index and cosine similarity. The Jaccard index, or the Jaccard similarity coefficient, was used to quantify the similarity between two sets. It is defined as the ratio of the size of the intersection of the two sets to the size of their union. The Jaccard index (J) is expressed as

$$J(A,B) = \frac{|A \cap B|}{|A \cup B|}$$

where A and B represent the two sets being compared (spike activity for ripple A vs ripples B), |A∩B| is the number of elements in the intersection of the sets, and |A∪B| is the number of elements in the union of the sets. The resulting value ranges from 0 to 1. Similarly, cosine similarity, which quantifies the cosine of the angle between two vectors, was used to measure the similarity between two spike vectors. Cosine similarity is given by

$$CS = \frac{A \cdot B}{\| A \| \| B \|}$$

where A and B are the two vectors being compared, $A \cdot B$ is the dot product, and $\| A \|$ and $\| B \|$ represent the magnitudes of the vectors. The values range from -1 to 1 where 1 indicates identical vectors and -1 indicates that the vectors have an angular difference of 180 degrees. Actual spike counts were used for cosine similarity calculation.

Assembly detection

To detect cell assemblies in CA1 and PFC populations, a previously described method was used.[93,94] Significant cofiring patterns in CA1 or PFC were detected using a method based on principal and independent component analyses. For each W-Track epoch, the spike trains of each neuron were binned into 20 ms time windows (excluding CA1 ripple times) and Z-scored to eliminate any biases due to differences in firing rates. Principal component analysis was then applied to the Z-scored spike matrix (Z). The resulting eigenvalue decomposition of the correlation matrix (C) was given by:

$$\sum_{i=1}^{n} \lambda_i \, p_i p_i^T = C$$

Where p_i is the ith principal component of C and λ_i is the corresponding eigenvalue. Note that $C = \frac{1}{n} Z Z^T$ is the correlation matrix of Z. To determine the number of significant coactivity patterns in the data, the Marcenko-Pastur law was used to calculate a threshold eigenvalue λ_{max}, which was given by $\lambda_{max} = \left(1 + \sqrt{n/B}\right)^2$, where n is the number of recorded units and B is the total number of bins. Note that an eigenvalue exceeding λ_{max} indicates that the corresponding cell assembly explains more correlation than expected if the activity of neurons was independent of each other. The number of eigenvalues above λ_{max}, N_A, represents the number of significant patterns found in the data. These principal components were then projected back onto the original z-scored spike data:

$$Z_{PROJ} = P_{SIGN}^T Z$$

where P_{SIGN} is the nXN_A matrix with N_A columns. Independent component analysis (ICA, RobustICA)[95] was then used to identify patterns that were maximally independent from each other. ICA was applied to the matrix Z_{PROJ} to find an $N_A X N_A$ unmixing matrix, W, which was used to obtain the weights of each cell in each assembly.

$$V = P_{SIGN} W$$

Since the sign of the output of ICA is arbitrary, the signs of the weight vector were set such that the highest absolute weight was set to positive.

Assembly reactivation strength

To assess the reactivation of these detected assemblies during sleep sessions, the expression strength of each pattern over time was given by:

$$R_k(t) = z(t)^T P_k z(t)$$

$R_k(t)$ is the reactivation strength of assembly k at time t, $z(t)$ is the z-scored firing rate vector for all neurons at time t, and P_k is the projection matrix for assembly k, constructed by taking the outer product of its weight vector v_k. Additionally, the diagonal of the projection matrix was set to zero to reduce the influence of highly active neurons, and the reactivation strength was calculated such that only the positive weight cells were assessed. Thus, only patterns of coactivity are detected as periods of high reactivation strength. Only sleep sessions with a preceding run session to use as a template were included for reactivation analysis (sleep sessions 2-9).

Assembly sequence detection surrounding ripple events

The consistency of assembly reactivation surrounding REM HFEs was assessed by implementing a cross-validation process similar to procedures used for place cell sequences.[96,97] We employed a split-ripple procedure where ripple events were randomly split into two halves. The average reactivation strength for each assembly was then

calculated across all ripples across both halves separately. This was performed across all animals and epochs. The assemblies aligned to the first half were subsequently sorted by peak reactivation strength within a ±500 ms window around ripple times, and the assemblies aligned to the second half were sorted using the same sort indices such that each row in the two matrices correspond to the same assembly. The consistency of temporal assembly reactivation was quantified as the Pearson correlation between the peak reactivation strengths of the first and second halves. This procedure was conducted 1000 times using different subsets of ripples for the first and second halves to obtain a distribution or correlation coefficients. For comparison, a distribution of shuffled data was obtained by circularly shuffling assembly reactivation strength prior to ripple alignment, and the above procedure was performed.

Rank-order correlation

To evaluate the consistency with which populations of neurons in PFC fired in sequence during chained events, we calculated the rank-order correlation between each chain and its template as previously described.[98,99] The population activity during each ripple in a chained event was concatenated (inter-ripple activity excluded), and for each concatenated event with ≥5 cells active, the spiking activity was reduced to each unit's first spike time, chronologically ordered, and normalized from 0 to 1. Then, a cross-validated template-based method was used to calculate sequence similarity between each event and its template. For each event, a template was created by averaging the normalized rank of each cell across all events excluding the event in question. The rank correlation was reported as the mean Pearson correlation coefficient between the event and template across all events. For comparison, a null distribution was generated by jittering spike times (1000 jitters) and performing the rank-order analysis above.

2-D rate maps

2-D spatial rate maps during active behavior on the W-Track were calculated during periods of high mobility (>5 cm/s; all SWR times excluded) at positional bins where occupancy was >20 ms .Then, the 2-D spatial maps were calculated by dividing the binned spike count by the occupancy in each 1 cm^2 positional bin and smoothed with a Gaussian kernel (σ = 2).

Ripple cofiring

To quantify ripple cofiring during events, a pairwise coactivity z-score was calculated as previously described.[100] Briefly, this coactivity measure estimates how likely two cells will fire together during ripple events and is normalized by the incidence of spiking independent of the other cell:

$$Zcoactivity_{a,b} = \frac{n_{ab} - \frac{n_a n_b}{N}}{\sqrt{n_a n_b (N - n_a)(N - n_b)/\left(N^2(N-1)\right)}}$$

where N is the number of ripple events, n_a and n_b are the number of events where cell a and cell b were active, respectively, and n_{ab} is the number of events where both cells were active. The same procedure was used to calculate cofiring between pairs in the model simulations.

Change in firing rate across sleep

To assess differences in firing rate changes in CA1 and PFC over the course of sleep, populations were separated into low or high cross-regional cofiring units based on the z-scored coactivity metric above as well as the Pearson correlation between spike count vectors across all REM ripple chains or independent NREM ripples. Here, we are only including independent ripples for NREM analysis since we have shown that CA1-PFC coactivity is elevated when PFC ripples are coordinated with CA1 SWRs.[23] Exclusion of coordinated ripple events allows us to assess the influence of strictly PFC ripples in NREM on firing rate changes. Since we observed a bimodal distribution of CA1-PFC cofiring values, we split the population based on whether the average (across all cell-cell combinations) cofiring value or correlation coefficient of a cell was above or below 0. Since the NREM ripple cofiring distribution was unimodal, we additionally split the populations using the mean of the average cofiring or correlation coefficient distributions. For each cell, the change in the firing rate from the first bout to the last bout of NREM sleep was calculated and compared for low and high coactive cells. Only epochs that had first and last NREM bouts exceeding 30 s in length were included for analysis.

Network model

Computational simulations were done using a simplified model of a small cortical network. The model contains 1,600 excitatory pyramidal and 400 inhibitory interneuron modified Hodgkin-Huxley neurons laid out in a topographical grid. Connections are random, with probability of connection decaying with spatial distance on the grid. Connection probabilities were drawn from known layer 2/3 cortical connectivity rates of pyramidal cells and somatostatin (SST) interneurons. Synaptic weights were assigned randomly using log-normal distributions. Inhibitory cells in the model are regular-spiking with a voltage equation identical to pyramidal cells.

The voltage equation for the neuron model is:

$$C_M \frac{dV}{dt} = -m_\infty^3 h g_{Na}(V - E_{Na}) - n g_{Kdr}(V - E_K) - s g_{Ks}(V - E_K) - g_{leak}(V - E_{leak}) + I_{base} + I_{noise} - I_{syn} + I_{stim}$$

Where g_x are the maximal conductances, and each of the activation variables $h, n,$ and s have a differential equation of the form:

$$\frac{dy}{dt} = \frac{1}{\tau(V)}(y_\infty - y)$$

Where y_∞ are the steady state values for each of the gating variables, each a function of voltage.

For every presynaptic spike, the synaptic conductance between neurons is calculated as the difference between two decaying exponentials. Model pyramidal neurons and interneurons both elicit fast, large-amplitude synaptic inputs in connected postsynaptic cells modeled after glutamate and GABA-A receptors, respectively. Interneurons also elicit a slow, low-amplitude GABA-B-like conductance in connected neurons. In addition,

a white noise current I_{noise} is applied to each neuron separately to introduce random variation.

Both pyramidal neurons and interneurons in the model feature a slow potassium conductance, g_{Ks}, that is active at neuronal resting potential and modeled after the slow potassium M-current.[51,101] The biological effect of acetylcholine (ACh) on the M-current through the M1 muscarinic ACh receptor is recreated in the model by raising or lowering g_{Ks} to simulate decreases or increases, respectively, in ACh concentration. As in biological neurons, lowering g_{Ks} shifts model neurons from Type 2 excitability (resonators) to Type 1 excitability (integrators), raising their excitability but lowering their tendency to synchronize spiking when connected.[53] The result for a connected network of neurons is, in general, lower sensitivity to inputs and an increased propensity for synchronous spiking in simulations modeling a low ACh condition, but increased sensitivity and less correlated spiking in simulations modeling a high ACh condition, as is observed experimentally.[102,103] Model simulations of NREM sleep use $g_{Ks} = 1.5$ for all neurons, while simulations of REM sleep use $g_{Ks} = 0$. I_{base} is used to slightly hyperpolarize interneurons during REM to maintain balanced excitation and inhibition.

Each external stimulus input to the network I_{stim} is modeled as a depolarizing current injection to a random 30% of neurons. For the NREM brief stimuli, a gaussian profile that peaks at the midpoint of the stimulus was used, with duration drawn from a normal distribution with a mean of 70 ms and standard deviation 20 ms. Stimulus peak amplitude was calculated similarly, with a mean of 0.75 and standard deviation 0.3. For REM theta stimuli, the input was a sinusoid with frequency drawn from normal distribution with mean 8.5 Hz and 3 standard deviations within 7-10 Hz range. Stimulus amplitude was convolved with a gaussian profile peaking at the midpoint of the stimulus duration. Negative amplitude phases of the sinusoid were set to zero. For REM stimulus duration, mean 3000 ms and standard deviation 250 ms duration were used. Peak amplitude parameters were identical to NREM. No negative durations or amplitudes were allowed, and set to zero if drawn. Triggering of a stimulus event was determined by a Bernoulli process with a success rate of on average 1 Hz, with overlapping stimuli not permitted. For theta stimuli, a minimum delay of 1000 ms was enforced after the end of each stimulus to allow the network time to return to baseline activity.

QUANTIFICATION AND STATISTICAL ANALYSIS

All statistical analyses were performed with MATLAB (MathWorks, Natick, MA; R2022a) functions or custom scripts. No specific analysis was performed to predetermine sample size, but the number used in this study is similar to or larger than typically used. Nonparametric, two-tailed statistical tests (Wilcoxon rank-sum (WRS) and signed-rank (WSR), for unpaired and paired data, respectively) were used throughout the paper unless noted. $P < 0.05$ was considered the cutoff for statistical significance. Boxplots show the median (center line), interquartile range (box), and the furthest points not considered outliers (whiskers). Unless otherwise noted, values and errors in the text denote means ± SEM. p-values in the text are reported as follows: $p > 0.05$, $^{*}p < 0.05$, $^{**}p < 0.01$, $^{***}p < 0.001$.

ID	Epoch	NREM	REM	% REM	ID	Epoch	NREM	REM	% REM
	1	590	0	0.00%		1	715	121	14.47%
	2	574	0	0.00%		2	548	0	0.00%
	3	389	11	2.75%		3	1064	13	1.21%
	4	362	0	0.00%		4	1063	137	11.42%
JS17	5	629	0	0.00%	**BG1**	5	623	72	10.36%
	6	404	0	0.00%		6	1778	275	13.40%
	7	1197	10	0.83%		7	1636	263	13.85%
	8	1139	0	0.00%		8	1284	270	17.37%
	9	916	74	7.47%		9	693	27	3.75%
	1	414	11	2.59%		1	595	31	4.95%
	2	499	15	2.92%		2	49	0	0.00%
	3	836	36	4.13%		3	186	38	16.96%
	4	1124	0	0.00%		4	678	0	0.00%
JS13	5	1040	139	11.79%	**JS14**	5	605	0	0.00%
	6	1926	120	5.87%		6	901	167	15.64%
	7	1322	118	8.19%		7	661	86	11.51%
	8	1440	122	7.81%		8	594	126	17.50%
	9	1180	141	10.67%		9	814	95	10.45%
	1	8	0	0.00%		1	138	177	56.19%
	2	840	98	10.45%		2	750	158	17.40%
	3	497	275	35.62%		3	1066	124	10.42%
	4	1266	202	13.76%		4	863	128	12.92%
KL8	5	1571	113	6.71%	**JS21**	5	435	14	3.12%
	6	629	182	22.44%		6	649	0	0.00%
	7	1346	256	15.98%		7	818	23	2.73%
	8	1193	243	16.92%		8	859	13	1.49%
	9	568	41	6.73%		9	743	0	0.00%
	1	3	0	0.00%		1	54	0	0.00%
	2	76	12	13.64%		2	5	0	0.00%
	3	291	45	13.39%		3	133	0	0.00%
	4	145	0	0.00%		4	637	26	3.92%
JS34	5	238	15	5.93%	**JS12**	5	562	11	1.92%
	6	1513	274	15.33%		6	1319	114	7.96%
	7	453	69	13.22%		7	1178	83	6.58%
	8	535	75	12.30%		8	1333	190	12.48%
	9	1070	112	9.48%		9	720	0	0.00%

	1	731	30	3.94%		1	25	0	0.00%
	2	435	0	0.00%		2	504	16	3.08%
	3	742	0	0.00%		3	885	34	3.70%
	4	865	0	0.00%		4	919	14	1.50%
JS15	5	1115	191	14.62%	**ZT2**	5	1658	240	12.64%
	6	1476	0	0.00%		6	1484	151	9.24%
	7	938	116	11.01%		7	1573	47	2.90%
	8	1195	136	10.22%		8	1804	239	11.70%
	9	990	224	18.45%		9	716	12	1.65%

Table S1. Amount of NREM and REM sleep (in seconds) across all animals and epochs.

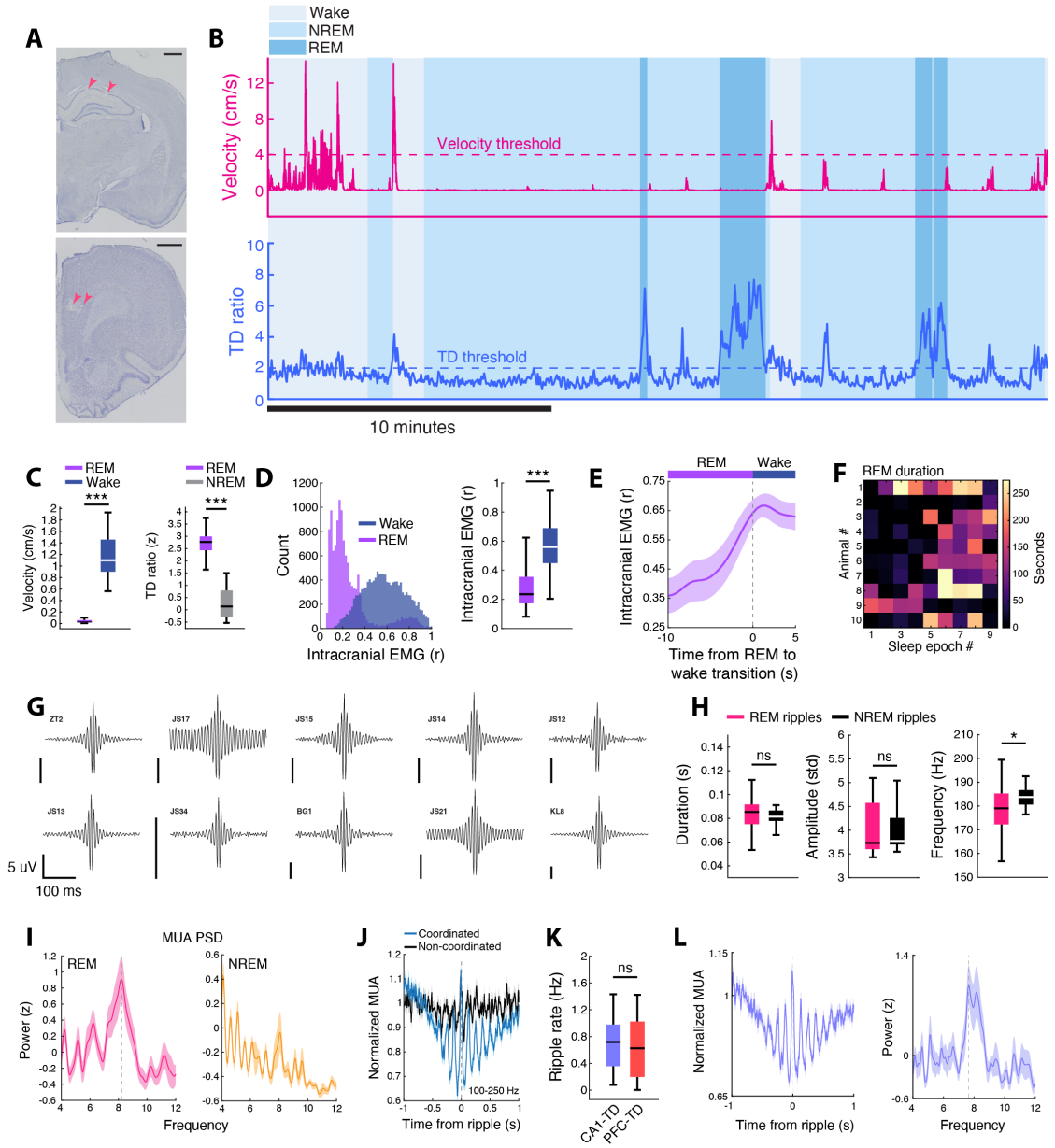

Figure S1. Characterization of REM sleep and prefrontal REM sleep ripples.

(**A**) Histological verification of recording locations in dorsal CA1 (Top) and PFC (Bottom). Red arrows indicate electrolytic lesions and scale bars represent 1 mm.
(**B**) Example sleep session showing each behavioral state detected using the sleep state algorithm that utilizes theta-to-delta ratio (TD ratio) and animal velocity (cm/s).
(**C**) (Left) Average velocity during wake and REM sleep (Wake = 1.16 ± 0.06 cm/s, REM = 0.05 ± 0.01 cm/s, *p = 5.39×10^{-7}, WSR). (Right) Theta-to-delta (TD) ratio in NREM and REM sleep (NREM = 0.30 ± 0.11, REM = 2.71 ± 0.10, ***p = 5.39×10^{-7}, WSR).
(**D**) Distributions of intracranial EMG values for wake and REM sleep. All 500 ms binned Pearson correlation values are shown.

(**E**) Comparison of the averaged intracranial EMG for bouts of wake and REM during all sleep epochs (Wake = 0.57 ± 0.01 , REM = 0.32 ± 0.02, ***p = 5.26×10^{-37}, WRS)
(**F**) Duration of REM sleep in each epoch (Total duration = 6089 s). Only epochs with at least 30 s of REM sleep were included for analysis.
(**G**) Average peak aligned amplitude plots across all detected REM ripple events for each animal.
(**H**) Comparison of ripple duration, amplitude (standard deviations above the mean), and frequency for NREM and REM ripples (Duration: NREM = 0.111 ± 0.017 ms, REM = 0.126 ± 0.030 ms, p = 0.59; Amplitude: NREM = 4.13 ± 0.12, REM = 4.23 ± 0.20, p = 0.31; Frequency: NREM = 184.96 ± 1.68 Hz, REM = 179.02 ± 1.82 Hz, *p = 0.018, WRS).
(**I**) Average power spectral density calculated from the REM and NREM ripple aligned multiunit activity in PFC. Note the peak around 8 Hz (theta frequency) for REM ripple aligned multiunit activity.
(**J**) PFC multiunit activity aligned to REM ripple events extracted from a wider frequency range (100-250 Hz). The separation into coordinated and non-coordinated events (Coordinated = 48.75 ± 2.6%) was determined by the overlap of these ripples with ripples extracted using the standard frequency range (150-250 Hz). This analysis was performed to demonstrate that the ripples extracted from the 150-250 Hz range primarily drives the theta frequency multiunit activity in PFC.
(**K**) PFC ripple rates during REM sleep extracted from either CA1 or PFC TD ratio. Ripple rates were similar during CA1 and PFC extracted REM sleep, validating the use of CA1-extracted REM sleep for further analysis.
(**L**) PFC multiunit activity and average power spectral density aligned to REM ripple events extracted from the overlap of CA1 and PFC REM sleep.

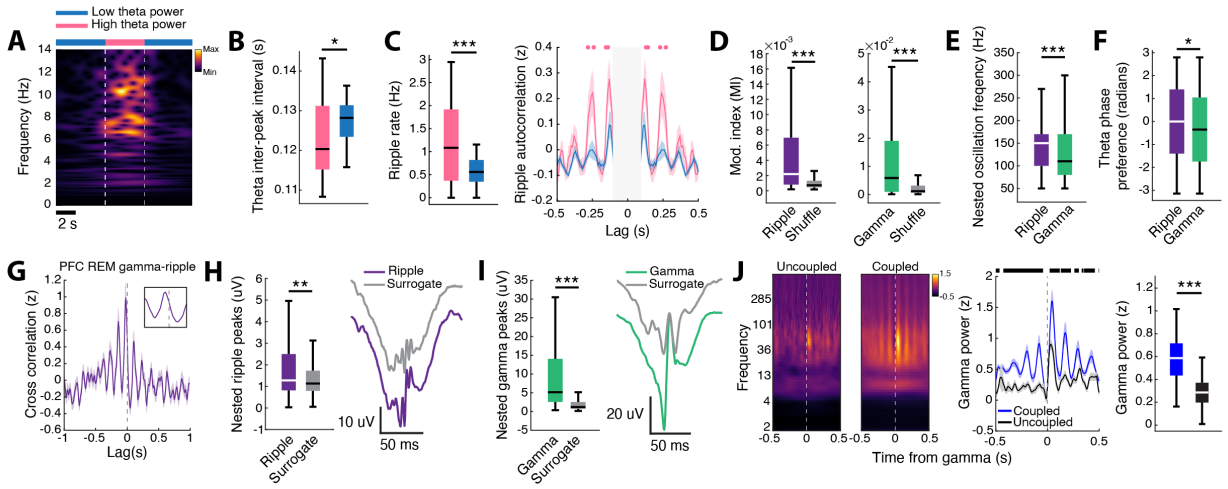

Figure S2. Coupling of gamma and ripple with PFC theta oscillations.

(**A**) Example showing bouts of low and high theta power within a REM sleep bout. High theta periods were bouts within REM that exceeded 4 standard deviations above the electrode averaged theta power in REM sleep for at least 900 ms.

(**B**) The CA1 theta inter-peak intervals (IPI) during high PFC theta power periods during REM sleep were lower (corresponding to higher theta frequency) than during low power periods, indicating that these high and low theta power periods may correspond to phasic and tonic substages of REM sleep, respectively (High theta IPI = 0.123 ± 0.002, Low theta IPI = 0.128 ± 8.3×10^{-4}, *p = 0.010, WRS).

(**C**) (Left) Rate of REM ripples during bouts of high or low theta power (High = 1.19 ± 0.15 Hz, Low = 0.58 ± 0.05 Hz, ***p = 1.33×10^{-4}, WSR). (Right) Ripple autocorrelation during periods of high or low theta power. Dots indicate bins where high and low theta power ripple autocorrelations differ (p<0.05, WRS).

(**D**) Modulation indices (MIs) for phase amplitude coupling (PAC) computed for ripple and gamma frequency oscillations compared to MIs calculated from circularly shifted theta phase and ripple/gamma amplitude vectors. Modulation was assessed for a phase frequency range from 2-12 Hz. The amplitude modulated frequencies were 150-250 Hz and 40-100 Hz for ripple and gamma, respectively (Ripple = 0.005 ± 3.21×10^{-4}, shuffle = 0.001 ± 8.94×10^{-5}, ***p = 1.13×10^{-31}; Gamma = 0.011 ± 6.49×10^{-4}, shuffle = 0.002 ± 1.67×10^{-4}, ***p = 2.97×10^{-24}, WRS).

(**E**) Frequency of the average theta nested oscillation either aligned to peak ripple or gamma power (See Methods). Note that aligning to peak ripple power at the preferred phase bin yields nested oscillations that are higher in frequency (Ripple = 146.48 ± 2.82, Gamma = 128.96 ± 3.091, ***p = 2.85×10^{-7}, WRS).

(**F**) Preferred theta phases of elevated ripple and gamma amplitude (Ripple = -0.13 ± 0.08 radians, Gamma = -0.38 ± 0.08 radians, *p = 0.016, WRS).

(**G**) Cross-correlation between PFC gamma and ripple events during REM sleep. The off-center peak at a negative lag (inset) indicates that gamma events tend to precede ripples, corroborating the phase preference difference in (**F**).

(**H**) Comparison of nested ripple peaks with a theta phase bin shuffled surrogate (See Methods; Ripple = 4.09 ± 0.48 μV, Surrogate = 1.92 ± 0.19 μV, **p = 0.0058, WRS).

(**I**) Same as in (**G**) but for gamma (Gamma = 11.33 ± 0.62 μV, Surrogate = 2.33 ± 0.20 μV, ***p = 9.46×10^{-94}, WRS).

(**J**) (Left) Gamma triggered spectrograms for events that were uncoupled or coupled to ripples. (Middle) Comparison of gamma power (40-100 Hz power ±500 ms from event onset) for uncoupled and coupled events. Note the oscillating gamma power during coupled events. (Right) Quantification of average ripple power for coupled and uncoupled events (Coupled = 0.60 ± 0.04, Uncoupled = 0.34 ± 0.03, ***p = 1.03×10^{-7}, WRS). Coupled gamma events were defined as gamma periods that were within 500 ms of a ripple event.

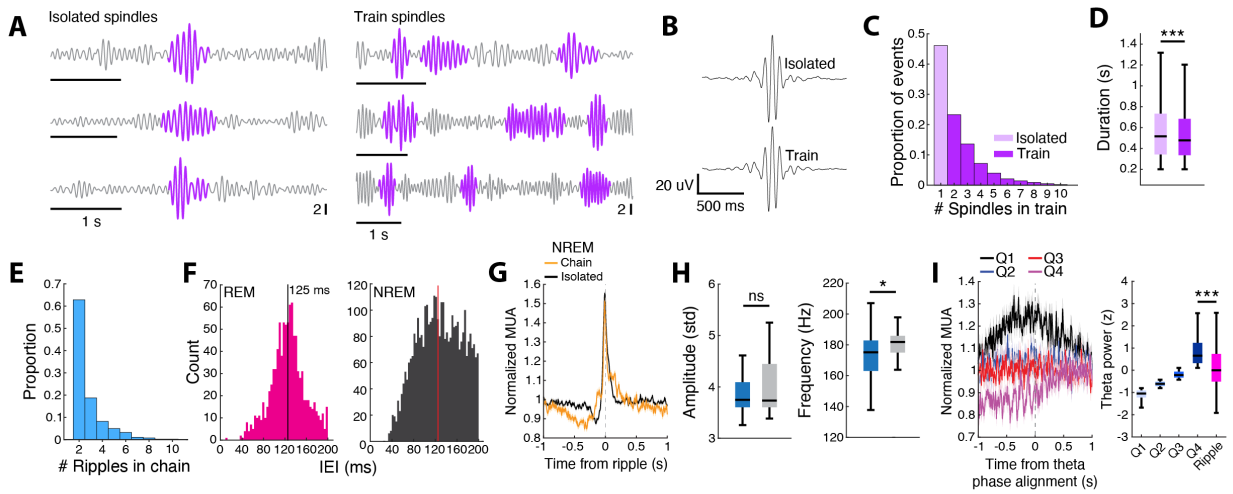

Figure S3. Chains of sleep oscillations in NREM (spindles) and REM (ripples) sleep.

(**A**) Example isolated and train spindles, similar to previous reports.[33]
(**B**) Averaged spindle peak aligned LFP for isolated and train spindles across all animals.
(**C**) Histogram displaying the proportions of NREM spindle train events of specific lengths (Compare with Darevsky et al., 2024).
(**D**) The durations of isolated and train spindles (Isolated = 0.579 ± 0.005 s, Train = 0.550 ± 0.003, ***p = 1.77×10^{-6}, WRS).
(**E**) Histogram displaying the proportions of REM ripple chain events of specific lengths.
(**F**) Histogram of all inter-event intervals (IEI) for ripple chains in (Left) REM or (Right) NREM sleep. Note the tight REM ripple IEI distribution centered around 125 ms, which corresponds to 8 Hz (theta frequency). Black and red vertical lines are displayed at 125 ms for both distributions.
(**G**) PFC multiunit activity aligned to chained and isolated NREM ripple events. Note the absence of theta modulated population activity during ripple chains in NREM sleep.
(**H**) Comparison of ripple amplitude and frequency for chained and isolated PFC REM ripples (Amplitude: Chain = 4.21 ± 0.26, Isolated = 4.17 ± 0.20, p = 0.995; Frequency: Chain = 172.54 ± 2.71 Hz, Isolated = 181.54 ± 1.51 Hz, *p = 0.018, WRS).
(**I**) (Left) PFC multiunit activity aligned to the preferred theta phase of REM ripples plotted according to theta power during surrogate events. (Right) Quantification of theta power in each quartile compared to the power during ripple events (Q1 = -1.10 ± 0.007, Q2 = -0.62 ± 0.004, Q3 = -0.20 ± 0.005, Q4 = 0.87 ± 0.024, Ripple = 0.26 ± 0.018, ***p = 5.74×10^{-114}, WRS).

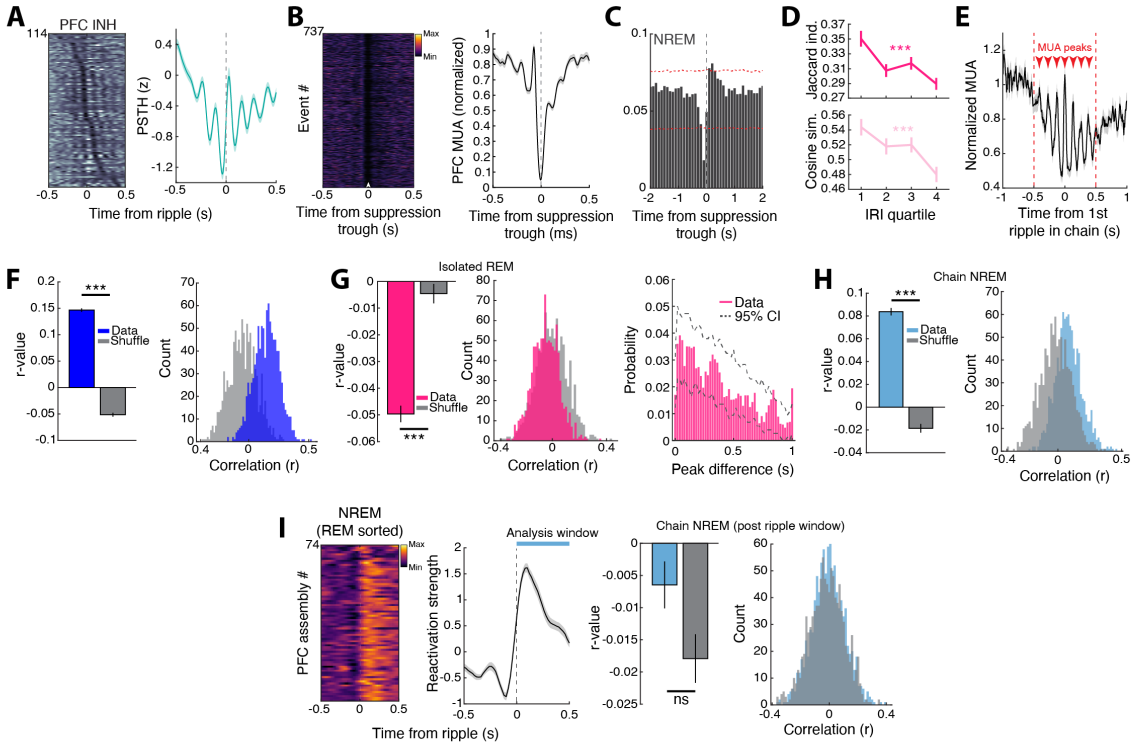

Figure S4. REM PFC ripples are associated with decreases in PFC activity and sequential reactivation as compared to NREM PFC ripples.

(**A**) PFC neurons that were negatively modulated (INH) during REM PFC ripple events (REM EXC modulation = 114). Although overall modulation in this subset of neurons surrounding PFC ripples is suppressive, there are transient peaks in activity that occur approximately 125 ms apart (8 Hz theta frequency).

(**B**) Extracted PFC population suppression events (Methods) aligned by their troughs. (Left) All example suppression events in an example epoch. (Right) Averaged PFC multiunit activity aligned to these events.

(**C**) The probability of NREM PFC ripples centered on population suppression events detected in NREM sleep. Unlike REM sleep, there is a decreased probability of NREM ripple occurrence surrounding suppression events, consistent with strong overall excitation during these events (**Figure 1I**). The slight peak to the right is likely reflective of the suppression in activity prior to the onset of NREM ripples (**Figure 1I**). The red dotted lines indicate the 99% confidence intervals based on suppression events extracted from shuffled multiunit activity.

(**D**) Relationship between IRI and (Top) Jaccard index and (Bottom) cosine similarity (Jaccard index, r = -0.094, ***p = 1.30×10^{-4}; Cosine similarity, r = -0.097, ***p = 7.16×10^{-5}, Pearson correlation).

(**E**) PFC multiunit activity aligned to the first ripple in each chained event. Note the peaks in the multiunit activity prior to the initial ripple within a chain, suggesting that fluctuations in PFC multiunit activity precede chained events. Thus, we aligned PFC reactivation strength to the first ripple in each chain for sequence cross-validation analysis.

(**F**) Cross-validation of the REM reactivation sequences surrounding gamma events (Data = 0.147 ± 0.003, Shuffle = -0.051 ± 0.004, ***p = 6.45×10^{-208}, WRS).

(**G**) (Left) Same as in (**C**) but for isolated REM ripples (Data = 0.050 ± 0.003, Shuffle = -0.005 ± 0.004, ***p = 4.82×10^{-4}, WRS). (Right) Probability of assembly peak displacement between randomly chosen halves of the isolated REM ripple aligned data. Note the absence of peaks at small displacements as seen in **Figure 4H**.

(**H**) Same as in (**C**) but for NREM ripple chains (Data = 0.084 ± 0.003, Shuffle = -0.019 ± 0.004, ***p = 1.37×10^{-75}, WRS).

(**I**) Cross-validation of the NREM reactivation sequences in the post ripple window (+500 ms from first chained ripple onset) (Data = -0.007 ± 0.004, Shuffle = -0.018 ± 0.004, p = 0.062, WRS).

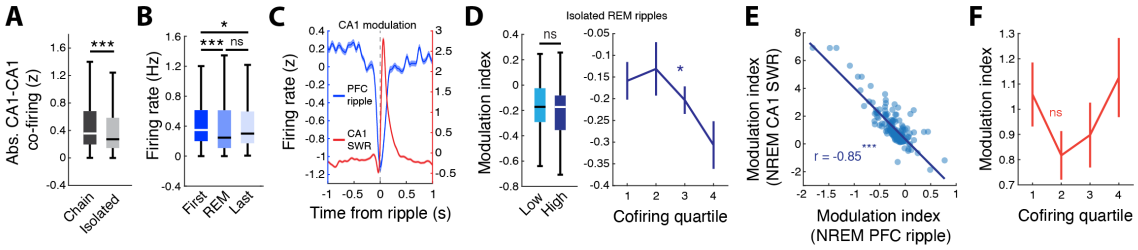

Figure S5. CA1 suppression during NREM PFC ripples and CA1 REM ripple cofiring.

(**A**) Absolute CA1-CA1 cell pair cofiring during chained and isolated ripples (Chain = 0.53 ± 0.02, Isolated = 0.48 ± 0.02, ***p = 1.42×10^{-4}, WRS). The magnitude of cofiring (positive and negative) was greater for ripple chains as compared to isolated ripples, suggesting differential engagement of CA1 neurons.

(**B**) Firing rates of CA1 pyramidal neurons during the first 30 s of NREM, REM, and the last 30 s of NREM sleep within an epoch (First 30 s NREM = 0.54 ± 0.04 Hz, REM = 0.51 ± 0.04 Hz , Last 30 s NREM = 0.51 ± 0.03, First vs REM, ***p = 1.10×10^{-4}, REM vs Last, p = 0.61, First vs Last, *p = 0.013, Friedman test with Bonferroni correction). CA1 firing rates decreased during REM and later in NREM.

(**C**) During NREM sleep, CA1 neurons were strongly suppressed during independent PFC ripples.

(**D**) (Left) There was no difference in the degree of suppression during NREM PFC ripples for low and high cofiring (during isolated REM ripples) CA1 neurons (Low cofiring = -0.16 ± 0.04, High cofiring = -0.21 ± 0.03, p = 0.40, WRS). (Right) The cofiring magnitude during isolated ripples was correlated with the degree of suppression during NREM PFC ripples, similar to REM ripple chains (r = -0.19, *p = 0.011, Pearson correlation).

(**E**) Correlation between CA1 modulation during independent NREM PFC ripples and coordinated SWRs. The more suppressed CA1 neurons are during PFC ripples, the stronger they are reactivated during coordinated SWRs (r = -0.85, ***p = 6.45×10^{-208}, Pearson correlation).

(**F**) There was no relationship between CA1 cofiring (with PFC) during REM ripple chains and the degree of modulation during coordinated SWRs in NREM sleep (r = 0.04, p = 0.44, Pearson correlation).

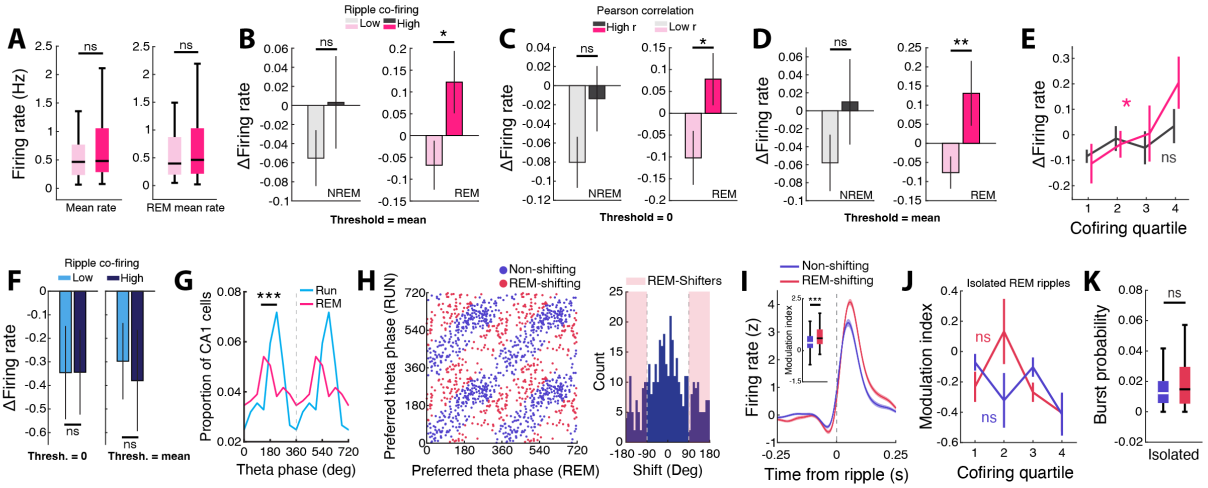

Figure S6. Relationship between REM PFC ripple cofiring, changes in CA1 firing rates over the course of sleep, and CA1 theta phase shifting neurons.

(**A**) (Left) Mean firing rates of high and low cofiring CA1 pyramidal neurons across the entire sleep epoch or (Right) restricted to REM sleep (Low cofiring mean rate = 0.69 ± 0.10, High cofiring mean rate = 0.79 ± 0.08, p = 0.41; Low cofiring REM mean rate = 0.73 ± 0.12, High cofiring REM mean rate = 0.78 ± 0.10, p = 0.49, WRS).

(**B**) (Left) Changes in CA1 firing rates from the first NREM bout to the last NREM bout within a sleep epoch plotted according to degree of cofiring (cofiring as measured by the z-scored cofiring metric; high, z-cofiring > mean of distribution; low, z-cofiring < mean of distribution) with PFC either during CA1-independent NREM or chained REM ripples in PFC (Low NREM = -0.06 ± 0.03, High NREM = 0.003 ± 0.048, p = 0.40; Low REM = -0.068 ± 0.056, High REM = 0.122 ± 0.071, *p = 0.013, WRS).

(**C**) Changes in CA1 firing rates from the first NREM bout to the last NREM bout within a sleep epoch plotted according to degree of cofiring (cofiring as measured by the Pearson correlation coefficient; high, r > 0; low, r < 0) with PFC either during CA1-independent NREM or chained REM ripples in PFC (Low NREM = -0.08 ± 0.03, High NREM = -0.01 ± 0.03, p = 0.080; Low REM = -0.10 ± 0.06, High REM = 0.08 ± 0.06, *p = 0.012, WRS).

(**D**) Same as in (**E**) but using above or below the mean of the cofiring distribution to designate high or low cofiring CA1 units, respectively (Low NREM = -0.06 ± 0.03, High NREM = 0.01 ± 0.05, p = 0.30; Low REM = -0.08 ± 0.04, High REM = 0.13 ± 0.08, **p = 0.002, WRS).

(**E**) Firing rate change separated by cofiring quartile. The change in CA1 firing rates over the course of sleep was correlated with PFC cofiring during REM ripples but not NREM ripples (NREM, r = 0.13, p = 0.49; REM, r = 0.17, *p = 0.029, Robust linear regression).

(**F**) Changes in PFC firing rates from the first NREM bout to the last NREM bout within a sleep epoch plotted according to degree of cofiring with CA1 during REM ripple chains in PFC. Results using 0 or the mean of the correlation coefficient distribution as the threshold shown on the left and right, respectively (0 threshold: Low = -0.35 ± 0.20, High = -0.34 ± 0.18, p = 0.90; Mean threshold: Low = -0.30 ± 0.21, High = -0.38 ± 0.21, p = 0.98, WRS).

(**G**) Preferred CA1 theta phase of CA1 neurons during running behavior or REM sleep. A subset of CA1 cells shifted their preferred theta phase during REM sleep (U^2 = 0.48, ***p

= 1.51×10^{-5}, Watson's U^2 test). Note that only cells that were significantly phase locked to the theta oscillation during both run and REM were used for analysis.

(**H**) (Left) Distributions of preferred CA1 theta phases during run and REM sleep. Only CA1 neurons with significant phase locking during both run and REM sleep were included for analysis. (Right) Histogram of theta phase shifts between run and the subsequent REM sleep session. Red shaded areas indicate neurons that had a phase shift >90°.

(**I**) (Left) SWR aligned firing rates of non-shifting and REM-shifting CA1 neurons. (Right) REM-shifting neurons had higher modulation indices, indicating stronger excitation during SWRs (Non-shifting = 0.60 ± 0.07, REM-shifting = 0.80 ± 0.07, ***p = 8.51×10^{-5},WRS)

(**J**) The cofiring magnitude during isolated REM ripples of non-shifting or REM-shifting CA1 neurons was not correlated with the degree of suppression during independent NREM PFC ripples (Non-shifting, r = -0.25, p = 0.085, REM-shifting, r = -0.32, p = 0.13, Pearson correlation).

(**K**) Burst probability of non-shifting and REM-shifting CA1 neurons during isolated REM ripples (Non-shifting = 0.015 ± 0.002, REM-shifting = 0.021 ± 0.003, p = 0.22, WRS).

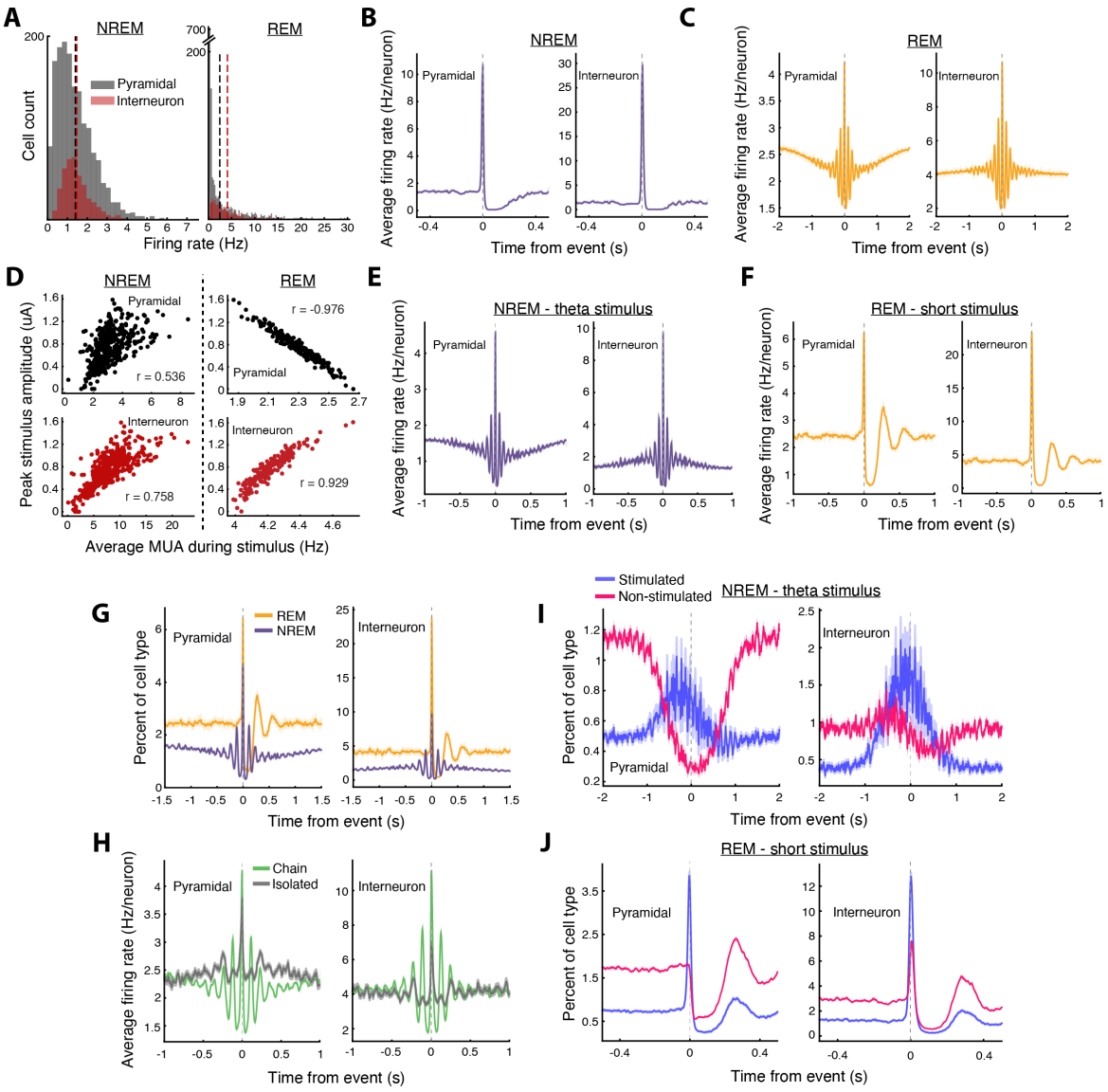

Figure S7. Model analyses split by cell type and reversed condition controls demonstrating the specific effects of ACh tone on network response.

(**A**) Firing rate histograms for NREM and REM simulations split by cell type. Bin size 0.25 Hz. NREM mean rate 1.41 Hz for pyramidal, 1.46 Hz for interneurons. REM mean rate 2.44 Hz for pyramidal, 4.14 Hz for interneurons.

(**B**) Average network firing rate surrounding NREM MUA peaks in stimulus periods, split by cell type.

(**C**) Same as (**B**), but for REM.

(**D**) Peak stimulus amplitude vs average MUA within the stimulus period split by cell type for NREM (Left) and REM (Right).

(**E**) Reversed stimulus condition for NREM. Same as (**B**), but swapping the stimulus profile by applying the REM theta-modulated stimulus profile during a low ACh (NREM) simulation. All other parameters are identical.

(**F**) Reversed stimulus condition for REM. Same as (**C**), but for a simulation using the brief NREM stimulus combined with high ACh (REM).

(**G**) Percent of each cell type with at least one spike in 10 ms bins for the swapped stimulus profile / ACh condition. Note the reduced breadth of pyramidal network activity when applying the brief stimulus in REM compared to NREM, compared to Main Figure 7B.
(**H**) Same as Main Figure 6G, but split by cell type.
(**I**) Swapped stimulus profile / ACh condition, applying the REM theta stimulus during a low ACh NREM simulation. Note the widespread recruitment of stimulated cells relative to non-stimulated cells, compared to REM response shown in Main Figure 7D.
(**J**) Same as (I), but applying the NREM brief stimulus during a high ACh REM simulation. Note the lack of peak in non-stimulated cell recruitment by the stimulus compared to NREM response shown in Main Figure 7C.

REFERENCES

1. Blumberg, M.S., Lesku, J.A., Libourel, P.A., Schmidt, M.H., and Rattenborg, N.C. (2020). What Is REM Sleep? Curr Biol *30*, R38-R49. 10.1016/j.cub.2019.11.045.
2. Peever, J., and Fuller, P.M. (2017). The Biology of REM Sleep. Curr Biol *27*, R1237-R1248. 10.1016/j.cub.2017.10.026.
3. Tempesta, D., Socci, V., De Gennaro, L., and Ferrara, M. (2018). Sleep and emotional processing. Sleep Med Rev *40*, 183-195. 10.1016/j.smrv.2017.12.005.
4. Mukai, Y., and Yamanaka, A. (2023). Functional roles of REM sleep. Neurosci Res *189*, 44-53. 10.1016/j.neures.2022.12.009.
5. Dauvilliers, Y., Schenck, C.H., Postuma, R.B., Iranzo, A., Luppi, P.H., Plazzi, G., Montplaisir, J., and Boeve, B. (2018). REM sleep behaviour disorder. Nat Rev Dis Primers *4*, 19. 10.1038/s41572-018-0016-5.
6. Squire, L.R., and Alvarez, P. (1995). Retrograde amnesia and memory consolidation: a neurobiological perspective. Curr Opin Neurobiol *5*, 169-177. 10.1016/0959-4388(95)80023-9.
7. Nadel, L., and Moscovitch, M. (1997). Memory consolidation, retrograde amnesia and the hippocampal complex. Curr Opin Neurobiol *7*, 217-227. 10.1016/s0959-4388(97)80010-4.
8. Buzsaki, G. (1989). Two-stage model of memory trace formation: a role for "noisy" brain states. Neuroscience *31*, 551-570. 10.1016/0306-4522(89)90423-5.
9. Staresina, B.P. (2024). Coupled sleep rhythms for memory consolidation. Trends Cogn Sci *28*, 339-351. 10.1016/j.tics.2024.02.002.
10. Buzsaki, G. (2015). Hippocampal sharp wave-ripple: A cognitive biomarker for episodic memory and planning. Hippocampus *25*, 1073-1188. 10.1002/hipo.22488.
11. Girardeau, G., and Zugaro, M. (2011). Hippocampal ripples and memory consolidation. Curr Opin Neurobiol *21*, 452-459. 10.1016/j.conb.2011.02.005.
12. Klinzing, J.G., Niethard, N., and Born, J. (2019). Mechanisms of systems memory consolidation during sleep. Nat Neurosci *22*, 1598-1610. 10.1038/s41593-019-0467-3.
13. Mizuseki, K., Diba, K., Pastalkova, E., and Buzsaki, G. (2011). Hippocampal CA1 pyramidal cells form functionally distinct sublayers. Nat Neurosci *14*, 1174-1181. 10.1038/nn.2894.
14. Tang, W., Shin, J.D., Frank, L.M., and Jadhav, S.P. (2017). Hippocampal-Prefrontal Reactivation during Learning Is Stronger in Awake Compared with Sleep States. J Neurosci *37*, 11789-11805. 10.1523/JNEUROSCI.2291-17.2017.
15. Boyce, R., Glasgow, S.D., Williams, S., and Adamantidis, A. (2016). Causal evidence for the role of REM sleep theta rhythm in contextual memory consolidation. Science *352*, 812-816. 10.1126/science.aad5252.
16. Montgomery, S.M., Sirota, A., and Buzsaki, G. (2008). Theta and gamma coordination of hippocampal networks during waking and rapid eye movement sleep. J Neurosci *28*, 6731-6741. 10.1523/JNEUROSCI.1227-08.2008.
17. Brankack, J., Scheffzuk, C., Kukushka, V.I., Vyssotski, A.L., Tort, A.B., and Draguhn, A. (2012). Distinct features of fast oscillations in phasic and tonic rapid eye movement sleep. J Sleep Res *21*, 630-633. 10.1111/j.1365-2869.2012.01037.x.
18. Bandarabadi, M., Boyce, R., Gutierrez Herrera, C., Bassetti, C.L., Williams, S., Schindler, K., and Adamantidis, A. (2019). Dynamic modulation of theta-gamma coupling during rapid eye movement sleep. Sleep *42*. 10.1093/sleep/zsz182.
19. Bueno-Junior, L.S., Ruckstuhl, M.S., Lim, M.M., and Watson, B.O. (2023). The temporal structure of REM sleep shows minute-scale fluctuations across brain and body in mice and humans. Proc Natl Acad Sci U S A *120*, e2213438120. 10.1073/pnas.2213438120.
20. Tort, A.B., Scheffer-Teixeira, R., Souza, B.C., Draguhn, A., and Brankack, J. (2013). Theta-associated high-frequency oscillations (110-160Hz) in the hippocampus and neocortex. Prog Neurobiol *100*, 1-14. 10.1016/j.pneurobio.2012.09.002.
21. Yamada, R.G., and Ueda, H.R. (2019). Molecular Mechanisms of REM Sleep. Front Neurosci *13*, 1402. 10.3389/fnins.2019.01402.
22. Khodagholy, D., Gelinas, J.N., and Buzsaki, G. (2017). Learning-enhanced coupling between ripple oscillations in association cortices and hippocampus. Science *358*, 369-372. 10.1126/science.aan6203.
23. Shin, J.D., and Jadhav, S.P. (2024). Prefrontal cortical ripples mediate top-down suppression of hippocampal reactivation during sleep memory consolidation. Curr Biol *34*, 2801-2811 e2809. 10.1016/j.cub.2024.05.018.

24. Vaz, A.P., Inati, S.K., Brunel, N., and Zaghloul, K.A. (2019). Coupled ripple oscillations between the medial temporal lobe and neocortex retrieve human memory. Science *363*, 975-978. 10.1126/science.aau8956.
25. van Schalkwijk, F.J., Weber, J., Hahn, M.A., Lendner, J.D., Inostroza, M., Lin, J.J., and Helfrich, R.F. (2023). An evolutionary conserved division-of-labor between archicortical and neocortical ripples organizes information transfer during sleep. Prog Neurobiol *227*, 102485. 10.1016/j.pneurobio.2023.102485.
26. Scheffzuk, C., Kukushka, V.I., Vyssotski, A.L., Draguhn, A., Tort, A.B., and Brankack, J. (2011). Selective coupling between theta phase and neocortical fast gamma oscillations during REM-sleep in mice. PLoS One *6*, e28489. 10.1371/journal.pone.0028489.
27. Maharjan, D.M., Dai, Y.Y., Glantz, E.H., and Jadhav, S.P. (2018). Disruption of dorsal hippocampal - prefrontal interactions using chemogenetic inactivation impairs spatial learning. Neurobiol Learn Mem *155*, 351-360. 10.1016/j.nlm.2018.08.023.
28. Shin, J.D., Tang, W., and Jadhav, S.P. (2019). Dynamics of Awake Hippocampal-Prefrontal Replay for Spatial Learning and Memory-Guided Decision Making. Neuron *104*, 1110-1125 e1117. 10.1016/j.neuron.2019.09.012.
29. Staresina, B.P., Niediek, J., Borger, V., Surges, R., and Mormann, F. (2023). How coupled slow oscillations, spindles and ripples coordinate neuronal processing and communication during human sleep. Nat Neurosci *26*, 1429-1437. 10.1038/s41593-023-01381-w.
30. Canolty, R.T., and Knight, R.T. (2010). The functional role of cross-frequency coupling. Trends Cogn Sci *14*, 506-515. 10.1016/j.tics.2010.09.001.
31. de Almeida-Filho, D.G., Koike, B.D.V., Billwiller, F., Farias, K.S., de Sales, I.R.P., Luppi, P.H., Ribeiro, S., and Queiroz, C.M. (2021). Hippocampus-retrosplenial cortex interaction is increased during phasic REM and contributes to memory consolidation. Sci Rep *11*, 13078. 10.1038/s41598-021-91659-5.
32. Davidson, T.J., Kloosterman, F., and Wilson, M.A. (2009). Hippocampal replay of extended experience. Neuron *63*, 497-507. 10.1016/j.neuron.2009.07.027.
33. Darevsky, D., Kim, J., and Ganguly, K. (2024). Coupling of Slow Oscillations in the Prefrontal and Motor Cortex Predicts Onset of Spindle Trains and Persistent Memory Reactivations. J Neurosci *44*. 10.1523/JNEUROSCI.0621-24.2024.
34. Antony, J.W., Piloto, L., Wang, M., Pacheco, P., Norman, K.A., and Paller, K.A. (2018). Sleep Spindle Refractoriness Segregates Periods of Memory Reactivation. Curr Biol *28*, 1736-1743 e1734. 10.1016/j.cub.2018.04.020.
35. Mallory, C.S., Widloski, J., and Foster, D.J. (2025). The time course and organization of hippocampal replay. Science *387*, 541-548. 10.1126/science.ads4760.
36. Judak, L., Chiovini, B., Juhasz, G., Palfi, D., Mezriczky, Z., Szadai, Z., Katona, G., Szmola, B., Ocsai, K., Martinecz, B., et al. (2022). Sharp-wave ripple doublets induce complex dendritic spikes in parvalbumin interneurons in vivo. Nat Commun *13*, 6715. 10.1038/s41467-022-34520-1.
37. Fries, P. (2005). A mechanism for cognitive dynamics: neuronal communication through neuronal coherence. Trends Cogn Sci *9*, 474-480. 10.1016/j.tics.2005.08.011.
38. Miyawaki, H., and Diba, K. (2016). Regulation of Hippocampal Firing by Network Oscillations during Sleep. Curr Biol *26*, 893-902. 10.1016/j.cub.2016.02.024.
39. Grosmark, A.D., Mizuseki, K., Pastalkova, E., Diba, K., and Buzsaki, G. (2012). REM sleep reorganizes hippocampal excitability. Neuron *75*, 1001-1007. 10.1016/j.neuron.2012.08.015.
40. Miyawaki, H., Watson, B.O., and Diba, K. (2019). Neuronal firing rates diverge during REM and homogenize during non-REM. Sci Rep *9*, 689. 10.1038/s41598-018-36710-8.
41. Valero, M., Cid, E., Averkin, R.G., Aguilar, J., Sanchez-Aguilera, A., Viney, T.J., Gomez-Dominguez, D., Bellistri, E., and de la Prida, L.M. (2015). Determinants of different deep and superficial CA1 pyramidal cell dynamics during sharp-wave ripples. Nat Neurosci *18*, 1281-1290. 10.1038/nn.4074.
42. Gu, L., Ren, M., Lin, L., and Xu, J. (2023). Calbindin-Expressing CA1 Pyramidal Neurons Encode Spatial Information More Efficiently. eNeuro *10*. 10.1523/ENEURO.0411-22.2023.
43. de la Prida, L.M. (2020). Potential factors influencing replay across CA1 during sharp-wave ripples. Philos Trans R Soc Lond B Biol Sci *375*, 20190236. 10.1098/rstb.2019.0236.
44. Harvey, R.E., Robinson, H.L., Liu, C., Oliva, A., and Fernandez-Ruiz, A. (2023). Hippocampo-cortical circuits for selective memory encoding, routing, and replay. Neuron *111*, 2076-2090 e2079. 10.1016/j.neuron.2023.04.015.

45. Sharif, F., Tayebi, B., Buzsaki, G., Royer, S., and Fernandez-Ruiz, A. (2021). Subcircuits of Deep and Superficial CA1 Place Cells Support Efficient Spatial Coding across Heterogeneous Environments. Neuron *109*, 363-376 e366. 10.1016/j.neuron.2020.10.034.
46. Poe, G.R., Nitz, D.A., McNaughton, B.L., and Barnes, C.A. (2000). Experience-dependent phase-reversal of hippocampal neuron firing during REM sleep. Brain Res *855*, 176-180. 10.1016/s0006-8993(99)02310-0.
47. Picciotto, M.R., Higley, M.J., and Mineur, Y.S. (2012). Acetylcholine as a neuromodulator: cholinergic signaling shapes nervous system function and behavior. Neuron *76*, 116-129. 10.1016/j.neuron.2012.08.036.
48. Eban-Rothschild, A., and de Lecea, L. (2017). Neuronal substrates for initiation, maintenance, and structural organization of sleep/wake states. F1000Res *6*, 212. 10.12688/f1000research.9677.1.
49. Colangelo, C., Shichkova, P., Keller, D., Markram, H., and Ramaswamy, S. (2019). Cellular, Synaptic and Network Effects of Acetylcholine in the Neocortex. Front Neural Circuits *13*, 24. 10.3389/fncir.2019.00024.
50. Roach, J.P., Ben-Jacob, E., Sander, L.M., and Zochowski, M.R. (2015). Formation and Dynamics of Waves in a Cortical Model of Cholinergic Modulation. PLoS Comput Biol *11*, e1004449. 10.1371/journal.pcbi.1004449.
51. Satchell, M., Butel-Fry, E., Noureddine, Z., Simmons, A., Ognjanovski, N., Aton, S.J., and Zochowski, M.R. (2025). Cholinergic modulation of neural networks supports sequential and complementary roles for NREM and REM states in memory consolidation. PLoS Comput Biol *21*, e1013097. 10.1371/journal.pcbi.1013097.
52. Czarnecki, P., Lin, J., Aton, S.J., and Zochowski, M. (2021). Dynamical Mechanism Underlying Scale-Free Network Reorganization in Low Acetylcholine States Corresponding to Slow Wave Sleep. Front Netw Physiol *1*. 10.3389/fnetp.2021.759131.
53. Stiefel, K.M., Gutkin, B.S., and Sejnowski, T.J. (2008). Cholinergic neuromodulation changes phase response curve shape and type in cortical pyramidal neurons. PLoS One *3*, e3947. 10.1371/journal.pone.0003947.
54. Gulledge, A.T., Bucci, D.J., Zhang, S.S., Matsui, M., and Yeh, H.H. (2009). M1 receptors mediate cholinergic modulation of excitability in neocortical pyramidal neurons. J Neurosci *29*, 9888-9902. 10.1523/JNEUROSCI.1366-09.2009.
55. Dasari, S., and Gulledge, A.T. (2011). M1 and M4 receptors modulate hippocampal pyramidal neurons. J Neurophysiol *105*, 779-792. 10.1152/jn.00686.2010.
56. Mishra, W., Kheradpezhouh, E., and Arabzadeh, E. (2024). Activation of M1 cholinergic receptors in mouse somatosensory cortex enhances information processing and detection behaviour. Commun Biol *7*, 3. 10.1038/s42003-023-05699-w.
57. Boyce, R., Williams, S., and Adamantidis, A. (2017). REM sleep and memory. Curr Opin Neurobiol *44*, 167-177. 10.1016/j.conb.2017.05.001.
58. Bollmann, L., Baracskay, P., Stella, F., and Csicsvari, J. (2025). Sleep stages antagonistically modulate reactivation drift. Neuron. 10.1016/j.neuron.2025.02.025.
59. Girardeau, G., Benchenane, K., Wiener, S.I., Buzsaki, G., and Zugaro, M.B. (2009). Selective suppression of hippocampal ripples impairs spatial memory. Nat Neurosci *12*, 1222-1223. 10.1038/nn.2384.
60. Maingret, N., Girardeau, G., Todorova, R., Goutierre, M., and Zugaro, M. (2016). Hippocampo-cortical coupling mediates memory consolidation during sleep. Nat Neurosci *19*, 959-964. 10.1038/nn.4304.
61. Chang, H., Tang, W., Wulf, A.M., Nyasulu, T., Wolf, M.E., Fernandez-Ruiz, A., and Oliva, A. (2025). Sleep microstructure organizes memory replay. Nature *637*, 1161-1169. 10.1038/s41586-024-08340-w.
62. Gridchyn, I., Schoenenberger, P., O'Neill, J., and Csicsvari, J. (2020). Assembly-Specific Disruption of Hippocampal Replay Leads to Selective Memory Deficit. Neuron *106*, 291-300 e296. 10.1016/j.neuron.2020.01.021.
63. Louie, K., and Wilson, M.A. (2001). Temporally structured replay of awake hippocampal ensemble activity during rapid eye movement sleep. Neuron *29*, 145-156. 10.1016/s0896-6273(01)00186-6.
64. Porter, B.S., Shi, C., Kozlova, E., and Jadhav, S.P. (2025). A novel rat spatial transitive inference paradigm for investigating memory schema and deliberation. bioRxiv, 2025.2008.2028.672785. 10.1101/2025.08.28.672785.
65. Abdou, K., Nomoto, M., Aly, M.H., Ibrahim, A.Z., Choko, K., Okubo-Suzuki, R., Muramatsu, S.I., and Inokuchi, K. (2024). Prefrontal coding of learned and inferred knowledge during REM and NREM sleep. Nat Commun *15*, 4566. 10.1038/s41467-024-48816-x.

66. Zeithamova, D., Schlichting, M.L., and Preston, A.R. (2012). The hippocampus and inferential reasoning: building memories to navigate future decisions. Front Hum Neurosci *6*, 70. 10.3389/fnhum.2012.00070.
67. Cairney, S.A., Durrant, S.J., Power, R., and Lewis, P.A. (2015). Complementary roles of slow-wave sleep and rapid eye movement sleep in emotional memory consolidation. Cereb Cortex *25*, 1565-1575. 10.1093/cercor/bht349.
68. Sanzeni, A., Akitake, B., Goldbach, H.C., Leedy, C.E., Brunel, N., and Histed, M.H. (2020). Inhibition stabilization is a widespread property of cortical networks. Elife *9*. 10.7554/eLife.54875.
69. Chen, N., Sugihara, H., and Sur, M. (2015). An acetylcholine-activated microcircuit drives temporal dynamics of cortical activity. Nat Neurosci *18*, 892-902. 10.1038/nn.4002.
70. Niethard, N., Hasegawa, M., Itokazu, T., Oyanedel, C.N., Born, J., and Sato, T.R. (2016). Sleep-Stage-Specific Regulation of Cortical Excitation and Inhibition. Curr Biol *26*, 2739-2749. 10.1016/j.cub.2016.08.035.
71. Ramirez-Villegas, J.F., Besserve, M., Murayama, Y., Evrard, H.C., Oeltermann, A., and Logothetis, N.K. (2021). Coupling of hippocampal theta and ripples with pontogeniculooccipital waves. Nature *589*, 96-102. 10.1038/s41586-020-2914-4.
72. Tsunematsu, T., Matsumoto, S., Merkler, M., and Sakata, S. (2023). Pontine Waves Accompanied by Short Hippocampal Sharp Wave-Ripples During Non-rapid Eye Movement Sleep. Sleep *46*. 10.1093/sleep/zsad193.
73. Teles-Grilo Ruivo, L.M., Baker, K.L., Conway, M.W., Kinsley, P.J., Gilmour, G., Phillips, K.G., Isaac, J.T.R., Lowry, J.P., and Mellor, J.R. (2017). Coordinated Acetylcholine Release in Prefrontal Cortex and Hippocampus Is Associated with Arousal and Reward on Distinct Timescales. Cell Rep *18*, 905-917. 10.1016/j.celrep.2016.12.085.
74. Nunez, A., and Buno, W. (2021). The Theta Rhythm of the Hippocampus: From Neuronal and Circuit Mechanisms to Behavior. Front Cell Neurosci *15*, 649262. 10.3389/fncel.2021.649262.
75. Goard, M., and Dan, Y. (2009). Basal forebrain activation enhances cortical coding of natural scenes. Nat Neurosci *12*, 1444-1449. 10.1038/nn.2402.
76. Zhang, Y., Cao, L., Varga, V., Jing, M., Karadas, M., Li, Y., and Buzsaki, G. (2021). Cholinergic suppression of hippocampal sharp-wave ripples impairs working memory. Proc Natl Acad Sci U S A *118*. 10.1073/pnas.2016432118.
77. Vandecasteele, M., Varga, V., Berenyi, A., Papp, E., Bartho, P., Venance, L., Freund, T.F., and Buzsaki, G. (2014). Optogenetic activation of septal cholinergic neurons suppresses sharp wave ripples and enhances theta oscillations in the hippocampus. Proc Natl Acad Sci U S A *111*, 13535-13540. 10.1073/pnas.1411233111.
78. Shin, J.D., Tang, W., and Jadhav, S.P. (2023). Protocol for geometric transformation of cognitive maps for generalization across hippocampal-prefrontal circuits. STAR Protoc *4*, 102513. 10.1016/j.xpro.2023.102513.
79. Schmitzer-Torbert, N., Jackson, J., Henze, D., Harris, K., and Redish, A.D. (2005). Quantitative measures of cluster quality for use in extracellular recordings. Neuroscience *131*, 1-11. 10.1016/j.neuroscience.2004.09.066.
80. Schomburg, E.W., Fernandez-Ruiz, A., Mizuseki, K., Berenyi, A., Anastassiou, C.A., Koch, C., and Buzsaki, G. (2014). Theta phase segregation of input-specific gamma patterns in entorhinal-hippocampal networks. Neuron *84*, 470-485. 10.1016/j.neuron.2014.08.051.
81. Watson, B.O., Levenstein, D., Greene, J.P., Gelinas, J.N., and Buzsaki, G. (2016). Network Homeostasis and State Dynamics of Neocortical Sleep. Neuron *90*, 839-852. 10.1016/j.neuron.2016.03.036.
82. Mitra, P., and Bokil, H. (2008). Observed brain dynamics (Oxford University Press).
83. Sullivan, D., Csicsvari, J., Mizuseki, K., Montgomery, S., Diba, K., and Buzsaki, G. (2011). Relationships between hippocampal sharp waves, ripples, and fast gamma oscillation: influence of dentate and entorhinal cortical activity. J Neurosci *31*, 8605-8616. 10.1523/JNEUROSCI.0294-11.2011.
84. Tort, A.B., Komorowski, R., Eichenbaum, H., and Kopell, N. (2010). Measuring phase-amplitude coupling between neuronal oscillations of different frequencies. J Neurophysiol *104*, 1195-1210. 10.1152/jn.00106.2010.
85. Vaz, A.P., Yaffe, R.B., Wittig, J.H., Jr., Inati, S.K., and Zaghloul, K.A. (2017). Dual origins of measured phase-amplitude coupling reveal distinct neural mechanisms underlying episodic memory in the human cortex. Neuroimage *148*, 148-159. 10.1016/j.neuroimage.2017.01.001.
86. Daume, J., Kaminski, J., Schjetnan, A.G.P., Salimpour, Y., Khan, U., Kyzar, M., Reed, C.M., Anderson, W.S., Valiante, T.A., Mamelak, A.N., and Rutishauser, U. (2024). Control of working memory by phase-amplitude coupling of human hippocampal neurons. Nature *629*, 393-401. 10.1038/s41586-024-07309-z.

87. Jadhav, S.P., Rothschild, G., Roumis, D.K., and Frank, L.M. (2016). Coordinated Excitation and Inhibition of Prefrontal Ensembles during Awake Hippocampal Sharp-Wave Ripple Events. Neuron *90*, 113-127. 10.1016/j.neuron.2016.02.010.
88. Nolte, G., Ziehe, A., Nikulin, V.V., Schlogl, A., Kramer, N., Brismar, T., and Muller, K.R. (2008). Robustly estimating the flow direction of information in complex physical systems. Phys Rev Lett *100*, 234101. 10.1103/PhysRevLett.100.234101.
89. Oostenveld, R., Fries, P., Maris, E., and Schoffelen, J.M. (2011). FieldTrip: Open source software for advanced analysis of MEG, EEG, and invasive electrophysiological data. Comput Intell Neurosci *2011*, 156869. 10.1155/2011/156869.
90. Siapas, A.G., Lubenov, E.V., and Wilson, M.A. (2005). Prefrontal phase locking to hippocampal theta oscillations. Neuron *46*, 141-151. 10.1016/j.neuron.2005.02.028.
91. Vinck, M., van Wingerden, M., Womelsdorf, T., Fries, P., and Pennartz, C.M. (2010). The pairwise phase consistency: a bias-free measure of rhythmic neuronal synchronization. Neuroimage *51*, 112-122. 10.1016/j.neuroimage.2010.01.073.
92. Harris, K.D., Hirase, H., Leinekugel, X., Henze, D.A., and Buzsaki, G. (2001). Temporal interaction between single spikes and complex spike bursts in hippocampal pyramidal cells. Neuron *32*, 141-149. 10.1016/s0896-6273(01)00447-0.
93. Peyrache, A., Khamassi, M., Benchenane, K., Wiener, S.I., and Battaglia, F.P. (2009). Replay of rule-learning related neural patterns in the prefrontal cortex during sleep. Nat Neurosci *12*, 919-926. 10.1038/nn.2337.
94. van de Ven, G.M., Trouche, S., McNamara, C.G., Allen, K., and Dupret, D. (2016). Hippocampal Offline Reactivation Consolidates Recently Formed Cell Assembly Patterns during Sharp Wave-Ripples. Neuron *92*, 968-974. 10.1016/j.neuron.2016.10.020.
95. Zarzoso, V., and Comon, P. (2010). Robust independent component analysis by iterative maximization of the kurtosis contrast with algebraic optimal step size. IEEE Trans Neural Netw *21*, 248-261. 10.1109/TNN.2009.2035920.
96. Plitt, M.H., and Giocomo, L.M. (2021). Experience-dependent contextual codes in the hippocampus. Nat Neurosci *24*, 705-714. 10.1038/s41593-021-00816-6.
97. Sosa, M., Plitt, M.H., and Giocomo, L.M. (2024). Hippocampal sequences span experience relative to rewards. bioRxiv. 10.1101/2023.12.27.573490.
98. Stark, E., Roux, L., Eichler, R., and Buzsaki, G. (2015). Local generation of multineuronal spike sequences in the hippocampal CA1 region. Proc Natl Acad Sci U S A *112*, 10521-10526. 10.1073/pnas.1508785112.
99. Valero, M., Viney, T.J., Machold, R., Mederos, S., Zutshi, I., Schuman, B., Senzai, Y., Rudy, B., and Buzsaki, G. (2021). Sleep down state-active ID2/Nkx2.1 interneurons in the neocortex. Nat Neurosci *24*, 401-411. 10.1038/s41593-021-00797-6.
100. Cheng, S., and Frank, L.M. (2008). New experiences enhance coordinated neural activity in the hippocampus. Neuron *57*, 303-313. 10.1016/j.neuron.2007.11.035.
101. Delmas, P., and Brown, D.A. (2005). Pathways modulating neural KCNQ/M (Kv7) potassium channels. Nat Rev Neurosci *6*, 850-862. 10.1038/nrn1785.
102. McCormick, D.A., Wang, Z., and Huguenard, J. (1993). Neurotransmitter control of neocortical neuronal activity and excitability. Cereb Cortex *3*, 387-398. 10.1093/cercor/3.5.387.
103. Meir, I., Katz, Y., and Lampl, I. (2018). Membrane Potential Correlates of Network Decorrelation and Improved SNR by Cholinergic Activation in the Somatosensory Cortex. J Neurosci *38*, 10692-10708. 10.1523/JNEUROSCI.1159-18.2018.